Design and Analysis of Broadband Metamaterial Absorbers for Mid Infrared Applications

A PROJECT REPORT

SUBMITTED IN PARTIAL FULFILLMENT OF THE REQUIREMENTS
FOR THE AWARD OF THE DEGREE
OF

MASTER OF SCIENCE
IN
PHYSICS

Submitted by

Bhavay Luthra (2k23/MSCPHY/13)

Under the supervision of

Dr. Kamal Kishor

DEPARTMENT OF APPLIED PHYSICS
DELHI TECHNOLOGICAL UNIVERSITY
(Formerly Delhi College of Engineering)
Bawana Road, Delhi 110042

JUNE, 2025

DEPARTMENT OF Applied Physics
DELHI TECHNOLOGICAL UNIVERSITY
(Formerly Delhi College of Engineering)
Bawana Road, Delhi-110042

<u>CANDIDATE'S DECLARATION</u>

I, Bhavay Luthra (2k23/PHY/13) hereby certify that the work which is presented in the Major Project-II/Research Work entitled in fulfillment of the requirement for the award of the Degree of Master of Science in Physics, and submitted to the Department of Applied Physics, Delhi Technological University, Delhi, is an authentic record of my/our own, carried out during a period from September 2024 to June 2025 under the supervision of Dr. Kamal Kishor.

The matter presented in this report/thesis has not been submitted by us/me for the award of any other degree of this or any other Institute/University. The work has been published/accepted/communicated in SCI/SCI Expanded/SSCI/Scopus indexed journal OR peer-reviewed Scopus indexed conference with the following details:

Title of the Paper: Broadband Multi-Patterned Metamaterial Absorber for Mid-Infrared Region

Author names (in sequence as per research paper): Bhavay Luthra, Ankit, Monu Nath Baitha, Kamal Kishor

Name of Conference/Journal: Journal of Electronic Materials

Conference Dates with venue (if applicable): March 3-5 2025, ARSD College, University of Delhi, India

Have you registered for the conference (Yes/No)?: Yes

Status of paper (Accepted/Published/Communicated): Under Review

Date of paper communication:

Date of paper acceptance:

Date of paper publication:

Place: Delhi   Bhavay Luthra

Date: dd.mm.yy   2k23/MSCPHY/13

DEPARTMENT OF APPLIED PHYSICS
DELHI TECHNOLOGICAL UNIVERSITY
(Formerly Delhi College of Engineering)
Bawana Road, Delhi-110042

<u>CERTIFICATE</u>

To the best of my knowledge, the above work bas not been submitted in part or full for any Degree or Diploma to this University or elsewhere. I, further certify that the publication and indexing information given by the students is correct.

Place: Delhi   Dr. Kamal Kishor

Date: dd.mm.yyyy   **SUPERVISOR**

DEPARTMENT OF APPLIED PHYSICS
DELHI TECHNOLOGICAL UNIVERSITY
(Formerly Delhi College of Engineering)
Bawana Road, Delhi-110042

<u>ACKNOWLEDGEMENT</u>

I wish to express our sincerest gratitude to Dr. Kamal Kishor for his continuous guidance and mentorship that he provided us during the project. He showed us the path to achieve our targets by explaining all the tasks to be done and explained to us the importance of this project as well as its industrial relevance. He was always ready to help us and clear our doubts regarding any hurdles in this project. Without his constant support and motivation, this project would not have been successful.

Place: Delhi   Bhavay Luthra

Date: dd.mm.yy   2k23/MSCPHY/13

Abstract

In this study, we present the design and analysis of a mid infrared metamaterial absorber based on a metal dielectric metal (MDM) configuration. The unit cell consists of an outer frame featuring a top triangular section with a cut on the bottom left corner, an L shaped boundary along the sides and bottom, and a central rectangle with an H shaped cavity. Gold (Au) is used as the metallic material, while silicon carbide (SiC) serves as the dielectric layer. The absorption spectrum was computed using the Finite Element Method (FEM) based COMSOL Multiphysics simulation software. The proposed design achieves over 98% absorption of incident light with a bandwidth of $0.7\,\mu\text{m}$ in TE mode. Additionally, the absorber demonstrates outstanding angular dependent absorption characteristics, maintaining over 90% absorption in the $3.7\text{-}4.2\,\mu\text{m}$ wavelength range for incident angles (ϕ) and elevation angles (θ). These properties make the proposed absorber highly suitable for applications such as polarimetric sensing and infrared detection systems.

Contents

List of Tables

List of Figures

List of Symbols

λ	Wavelength of electromagnetic radiation
$\vec{E}$	Electric field vector
$\vec{H}$	Magnetic field vector
$\vec{k}$	Wave vector (direction of propagation)
$\vec{S}$	Poynting vector (energy flux / power flow)
μ	Permeability
ϵ	Permittivity
∇	Nabla operator (used in $\nabla \times$ for curl)
$\tilde{\mu}$	Complex permeability
$\tilde{\varepsilon}$	Complex permittivity
ω	Angular frequency
j	Imaginary unit
$(-\vec{H})$	Negative magnetic field vector (used in left-handed system)
$(-\vec{k})$	Negative wave vector (used in left-handed system)
$\vec{k}_x$	Transverse component of the wave vector $\vec{k}$
$\vec{k}_y$	Component of the wave vector $\vec{k}$
$\vec{x}$	Displacement from equilibrium position
m	Mass (e.g., in SHM context)
γ	Damping coefficient / scaling factor
k	Spring constant
$\vec{F}(t)$	External force as a function of time
m_e	Electron mass
$\vec{r}$	Displacement of charge / Position vector
Γ	Damping factor (in the electron model)
ω_0	Natural frequency
q	Electric charge
$\vec{r}(\omega)$	Fourier transform of displacement $\vec{r}$
$\vec{E}(\omega)$	Fourier transform of electric field
$\vec{\mu}(\omega)$	Electric dipole moment in frequency domain
$\vec{P}$	Polarization (volume-averaged dipole moment)
N	Number of dipoles per unit volume
$\vec{P}(\omega)$	Polarization in frequency domain
$\chi(\omega)$ / χ	Electric susceptibility
ω_p	Plasma frequency
$\varepsilon_r(\omega)$	Relative permittivity in frequency domain
η	Refractive index
μ_r	Relative permeability

ϵ_r	Relative permittivity
$\eta(\omega)$	Frequency-dependent refractive index
η_o	Real part of refractive index
κ	Imaginary part of refractive index / Chirality parameter
n	Scalar refractive index
$\vec{D}$	Electric displacement field
$\vec{B}$	Magnetic induction
$\vec{J}$	Electric current density
σ	Electrical conductivity
$[\epsilon]$	Permittivity tensor
$[\mu]$	Permeability tensor
$[\sigma]$	Conductivity tensor
ϵ_x, ϵ_y, ϵ_z	Components of permittivity tensor
ζ, ξ	Bi-isotropic coupling coefficients
ϵ_1, ϵ_2, ϵ_3	Nonlinear permittivity coefficients
ϕ	Azimuthal angle
θ	Angle of incidence
t_m	Thickness of metal layer
t_d	Thickness of dielectric layer
S_{11}	Reflection coefficient parameter
SRR	Split Ring Resonator
SPP	Surface Plasmon Polaritons
LSP	Localized Surface Plasmon
MP	Magnetic Polariton
FWHM	Full Width at Half Maximum
dB	Decibel scale
MNZ	μ-near-zero materials
SEM	Scanning Electron Microscope
TE	Transverse Electric mode
TM	Transverse Magnetic mode
FEM	Finite Element Method
FDTD	Finite Difference Time Domain
TLM	Transmission Line Method
EBG	Electromagnetic Band Gap
FSS	Frequency Selective Surface
SiC	Silicon Carbide
CAD	Computer-Aided Design
COMSOL	Multiphysics simulation software

Chapter 1

INTRODUCTION

1.1 What are Metamaterials?

Wikipedia defines metamaterials as: "A metamaterial (from the Greek word *meta*, meaning "beyond" or "after", and the Latin word *materia*, meaning "matter" or "material") is a type of material engineered to have a property, typically rarely observed in naturally occurring materials, that is derived not from the properties of the base materials but from their newly designed structures."

In very simple terms, they are materials that derive their properties from structure rather than the type of material they are composed of. In metamaterials, the molecules that are typically the main type of component of any material are replaced by man-made structures. It have dimensions that depend on the λ of incident the electromagnetic radiation. So, for example, if the visible light is incident, then the dimensions of the metamaterial are of the order of nanometers, and in the case of GHz radiation, the size of the metamaterial may be as large as a few millimeters.
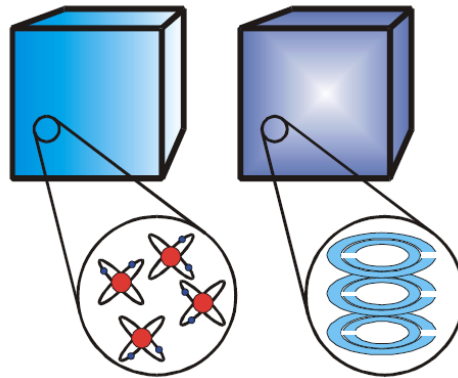
Figure 1.1: On the left we have a normal material made from constituent atoms, and on the right we have a metamaterial made from sub-units which may contain many atoms. Source: [1].

1.2 Evolution of Metamaterials

The idea of a metamaterial dates back more than fifty years. The idea was first discussed by Victor Veselago in 1968, who studied the effect of negative permeability and permittivity on wave propagation.[18]. However the term itself is more recent as it originated

in 1999 with the work of Rodger Walser.[19] The realization of the concept was in 1996 when wire structures were used to achieve negative permittivity, then in 1999 split-ring resonators were used to achieve negative permeability. Following this materials with a negative refractive index, i.e. both negative permittivity and negative permeability were constructed.

The area advanced quickly from the mid 1990s to the mid 2010s, which is why this period is referred to as the modern metamaterial era. For instance, construction of graded index metamaterials that allow controlled refraction of electromagnetic waves and can be used for lenses and for cloaking and development of theory of controlling wave propagation through optical transformations via metamaterials also advanced quickly.

By 2010 the concept had been extended to sound waves with the development of acoustic metamaterials and metasurfaces, with structures resembling membranes, coiled-up geometries, and Helmholtz resonators. Then in 2015 the dynamic metamaterials were created that can be for imaging and signal processing.

Metamaterials have been applied to increasingly specialized areas. For example in 2019 monolayers and two dimensional metamaterials were developed for electromagnetic absorbers in the terahertz range, and by 2020 tunnel resonators and chiral metamaterials had been used to manipulate microwaves. Advanced nano-structures such as copper plasmonic structures, and silicon-cored tungsten nanowires were applied to solar energy harvesting in 2021.

The last fifty years have seen metamaterials established as a key technology in the fields of physics, engineering, and materials science, with many widely varied applications.[2]
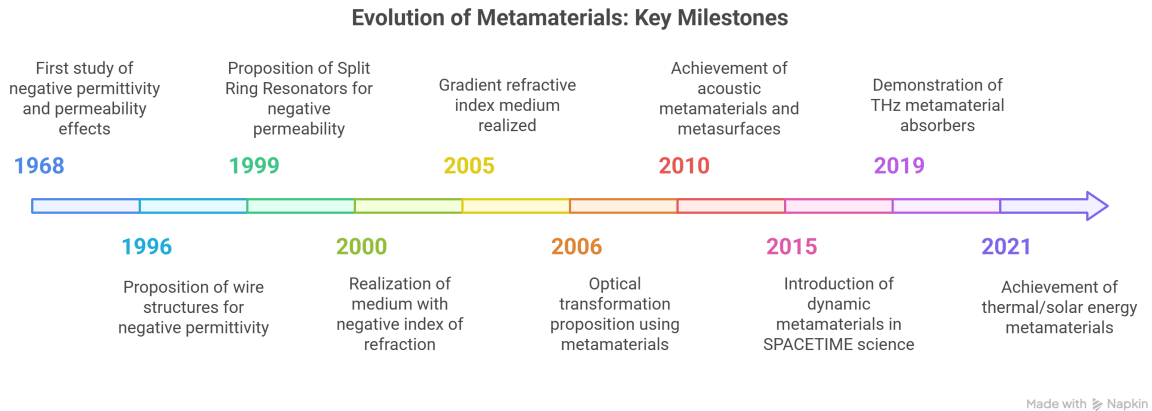
Figure 1.2: Evolution of metamaterial. Source: Image adapted from [2].

1.3   Lorentz Oscillator Model

When we discuss about properties of metamaterials, we study their response to electromagnetic radiation (i.e., their response curve). However, in order to study the response curve for metamaterials, we should be first familiar with the response curve of dielectrics. The response curve of ordinary materials can be described by the Lorentz (for dielectrics) and Drude (for metals) models. Both of these are classical models where it is assumed that electrons revolve in orbits around a heavy nucleus and move just like a spring-mass system with damping when subjected to an external field. For a metamaterial, the

combined Drude-Lorentz model describes the effective electromagnetic response of the metamaterial.[20]

When discussing optical response, for conventional materials, we study its permittivity only. This is because the relative permeability at optical frequencies is essentially unity.[21] Conversely, metamaterials allow us to control both the permittivity (ϵ_r) and permeability (μ_r).[22]. This unlocks a whole new range of applications such as super-lens (negative refraction) and perfect absorbers (impedance matching).
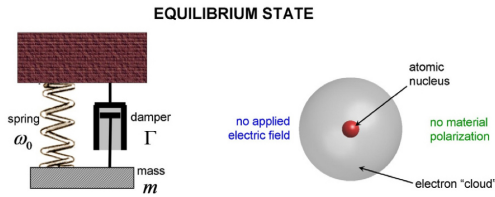
Figure 1.3: The neutral atom is equivalent to the spring–mass system at equilibrium. Source: [3]
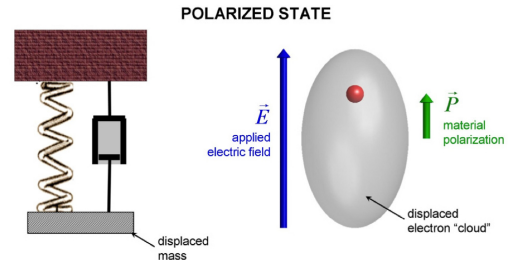
Figure 1.4: The polarized atom is equivalent to the spring–mass system at a non-equilibrium position. Source: EM-PossibleLecture13 [3]

Mathematical Analysis

A brief summary of the analysis follows. The complete derivation can be found in standard texts.

1. **General Equation of Simple Harmonic Motion (SHM):**

$$m\ddot{\vec{x}} + \gamma\dot{\vec{x}} + k\vec{x} = \vec{F}(t),$$

where m is the mass, $\vec{x}$ the displacement, γ the damping coefficient, k the spring constant, and $\vec{F}(t)$ the external force.

2. **Equation of Motion for a Bound Charge:** For a charge q in a time-varying electric field $\vec{E}$,

$$m_e\ddot{\vec{r}} + m_e\Gamma\dot{\vec{r}} + m_e\omega_0^2\vec{r} = -q\vec{E}.$$

3. **Fourier Transform:**

$$\vec{r}(\omega) = -\frac{q\vec{E}(\omega)}{m_e\left(\omega_0^2 - \omega^2 - j\omega\Gamma\right)}.$$

4. **Electric Dipole Moment:**

$$\vec{\mu}(\omega) = q\vec{r}(\omega) = \frac{q^2\vec{E}(\omega)}{m_e\left(\omega_0^2 - \omega^2 - j\omega\Gamma\right)}.$$

5. **Polarization:** With N dipoles per unit volume,

$$\vec{P}(\omega) = N\vec{\mu}(\omega).$$

6. **Material Susceptibility:**

$$\chi(\omega) = \frac{\omega_p^2}{\omega_0^2 - \omega^2 - j\omega\Gamma},$$

3

where $\omega_p^2 = Nq^2/(m_e \varepsilon_0)$.

7. **Dielectric Function:**

$$\tilde{\varepsilon}(\omega) = 1 + \chi(\omega) = 1 + \frac{\omega_p^2}{\omega_0^2 - \omega^2 - j\omega\Gamma}.$$

8. **Refractive Index:** For nonmagnetic materials ($\mu_r = 1$),

$$\eta(\omega) = \sqrt{\varepsilon_r(\omega)}.$$

Figure 1.5: Variation of refractive index with ω/Γ. The region between 10 and 20 is anomalous dispersion, where the real part decreases with increasing frequency. Source: [4]
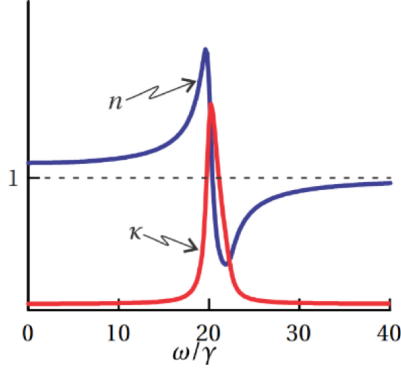
The region between 10 and 20 is called the anomalous region, as the real part of the refractive index decreases with an increase in frequency. Conversely, normal dispersion corresponds to regions where the real part increases with frequency. Around $\omega/\Gamma = 20$, we see a spike in the imaginary part of the refractive index, indicating maximum absorption (loss). As $\omega \to \infty$, $\eta_o \to 1$ and $\kappa \to 0$, so at high frequencies the overall refractive index tends to unity.

Chapter 2

A Taxonomy of Metamaterials and Their Applications

2.1 Classification of Metamaterials

2.1.1 On the basis of μ and ϵ
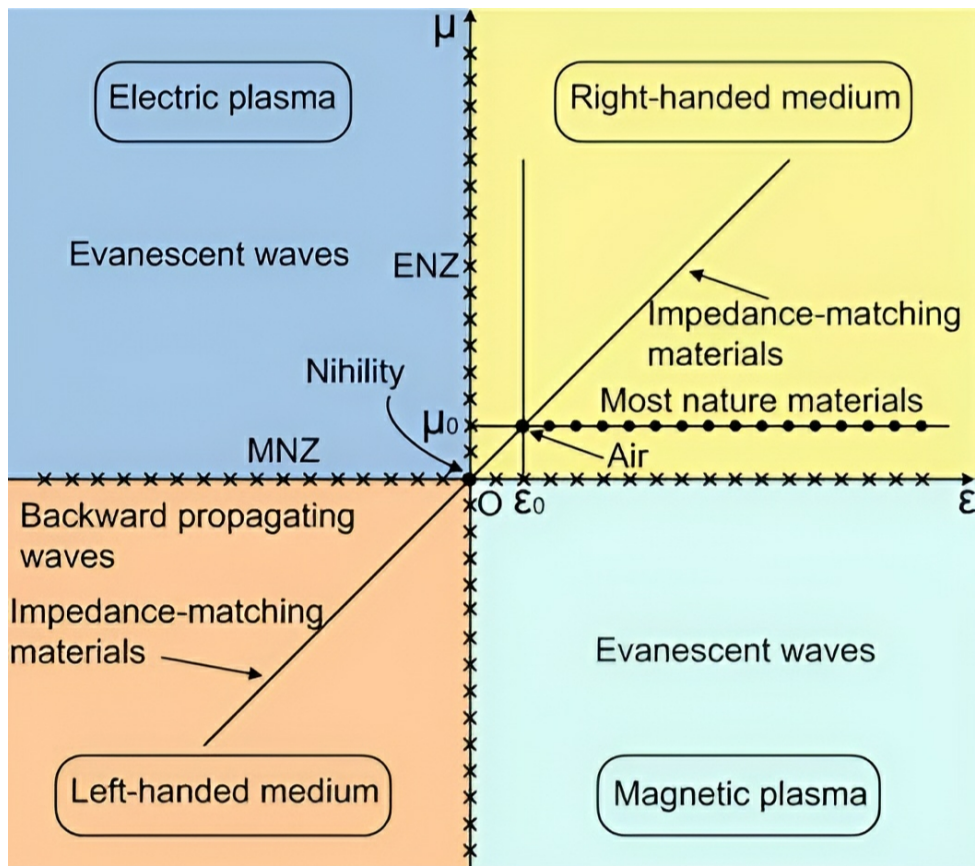
Figure 2.1: Classification of materials in the ϵ–μ domain. Source: Picture from [5]

1. **Double Positive (DPS) Material**: First quadrant where $\mu > 0$ and $\epsilon > 0$. It comprises all right-handed materials (RHM) or ordinary materials, which support forward-propagating waves.

2. **Epsilon Negative (ENG) Material**: Second quadrant, where $\mu > 0$ but $\epsilon < 0$. Electric plasma, which supports evanescent waves, falls under this category.

3. **Mu Negative (MNG) Material**: Fourth quadrant, where $\mu < 0$ but $\epsilon > 0$. Magnetic plasma, which supports evanescent waves, lies in this region. Gyrotropic natural materials in radio frequency have a negative real part of the permeability. Split-ring structures also shows this behavior.

4. **Double Negative (DNG) Material**: Third quadrant where $\mu < 0$ and $\epsilon < 0$. Materials in this quadrant form a left-handed system and support backward-propagating waves (negative $\vec{k}$).

Origin (the point $\mu = 0$, $\epsilon = 0$) is called **nihility**. The term **MNZ** stands for μ-*near-zero* materials.

Left-Handed Metamaterials

All ordinary materials are right-handed. For ordinary materials $\vec{E}$, $\vec{H}$, and $\vec{k}$ form a right-handed system meaning the direction of propagation of the wave, represented by $\vec{k}$, is perpendicular to both $\vec{E}$ and $\vec{H}$ and satisfies the relation:

$$\vec{k} = \vec{E} \times \vec{H},$$

so that $\vec{E} \perp \vec{H}$, $\vec{H} \perp \vec{k}$, and $\vec{k} \perp \vec{E}$ However, this is not the case in DNG metamaterials. DNG Metamaterials are left-handed in nature.

The reason they are left hand is because μ and ε are negative. This can be shown by substituting the negative values of μ and ε in Maxwell's equations:

$$\nabla \times \vec{E} = -j\omega(-\tilde{\mu})\vec{H}, \quad \nabla \times \vec{H} = j\omega(-\tilde{\varepsilon})\vec{E}.$$

Rewriting,

$$\nabla \times \vec{E} = -j\omega\tilde{\mu}(-\vec{H}), \quad \nabla \times (-\vec{H}) = j\omega\tilde{\varepsilon}\vec{E}.$$

The system is left-handed!

$$\vec{k} \perp \vec{E} \perp (-\vec{H}), \quad -\vec{k} \perp \vec{E} \perp \vec{H}.$$

$\vec{E}$, $\vec{H}$, and $\vec{k}$ form a "left-handed" system.

An important implication of this is, that the Poynting vector $\vec{S}(= \vec{E} \times \vec{B})$, which represents the direction of energy flow, is opposite to the wave vector $\vec{k}$. To illustrate this concept, consider the figure 2.2:
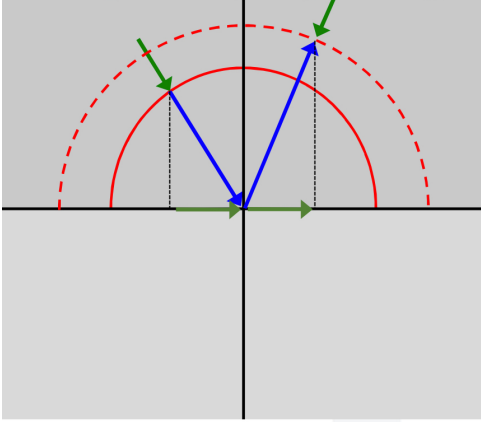
Figure 2.2: Electromagnetic wave refraction at an ordinary material-metamaterial interface, showing wave vector ($\vec{k}$) (blue) and Poynting vector ($\vec{S}$) (green) in the incident region. Source: [3]

1. On the top half, we have the ordinary material, and on the bottom half, we have the metamaterial.

2. On the right side of the normal material, $\vec{S}$ and $\vec{k}$ point in the same direction.

3. When $\vec{k}$ hits the interface, its transverse component ($\vec{k_x}$) should be continuous.

4. Since $\vec{k_x}$ is the same, $\vec{k_y}$ must be negative.

5. Causality ensures that the Poynting vector points in the direction of forward energy propagation, even in left-handed materials where the wave vector and energy flow are reversed.

2.1.2 On the basis of functional properties

On the basis of electromagnetic response mechanism and application domain, metamaterials can be broadly classified into seven types:

1. Electromagnetic Metamaterials

2. Chiral Metamaterials

3. Terahertz Metamaterials

4. Photonic Metamaterials

5. Tunable Metamaterials

6. Frequency Selective Surface (FSS) based Metamaterials

7. Nonlinear Metamaterials

Electromagnetic Metamaterials

Metamaterials that are specifically engineered to control and manipulate the amplitude, phase, polarization, frequency, and wave vector of electromagnetic waves. They have many practical applications from optical to microwave, such as band-pass filters, lenses, and microwave couplers. They can be further subdivided into:

1. Single Negative Metamaterials: One of μ or ϵ is negative.

2. Double Negative Metamaterials: Both μ and ϵ are negative.

3. Electromagnetic Band Gap (EBG) Metamaterials

4. Bi-isotropic and Bi-anisotropic Metamaterials

The first two have been discussed in the previous section.

Electromagnetic Band Gap (EBG): They are typically designed by placing dielectric substrate on a periodic metal patches. It can control the propagation of light by preventing certain frequencies via destructive interference while simultaneously reflecting any incident electromagnetic wave with no phase shift. This is implemented with photonic crystals or left-handed metamaterials. Due to this property, they are widely use to improve antennas quality and in building filters and miniaturized microwave devices.

Bi-isotropic and Bi-anisotropic Metamaterials: In isotropic media, $\vec{D}$, $\vec{B}$, and $\vec{J}$ are independent of the field direction.

$$\vec{D} = \epsilon\vec{E}, \quad \vec{B} = \mu\vec{H}, \quad \vec{J} = \sigma\vec{E}$$

where ϵ, μ, and σ are scalar. However, In anisotropic media, they depend on direction:

$$\vec{D} = [\epsilon]\vec{E}, \quad \vec{B} = [\mu]\vec{H}, \quad \vec{J} = [\sigma]\vec{E},$$

where $[\epsilon]$, $[\mu]$, and $[\sigma]$ are tensors. Double, single, double positive are based at the presumption of metamaterial that is exhibits independent electric as well as magnetic response.

Bi-isotropy introduces coupling between electric and magnetic fields.

$$\vec{D} = \epsilon\vec{E} + \zeta\vec{H}, \quad \vec{B} = \mu\vec{H} + \xi\vec{E}.$$

If ϵ, μ, ζ, and ξ are scalars, the medium is **bi-isotropic**; if they are tensors, it is **bi-anisotropic**. A similar coupling takes place in the electromagnetic metamaterial, where magnetic field produces an electrical polarization, which is known as magneto-electric coupling, and the electric field creates a magnetic polarization.
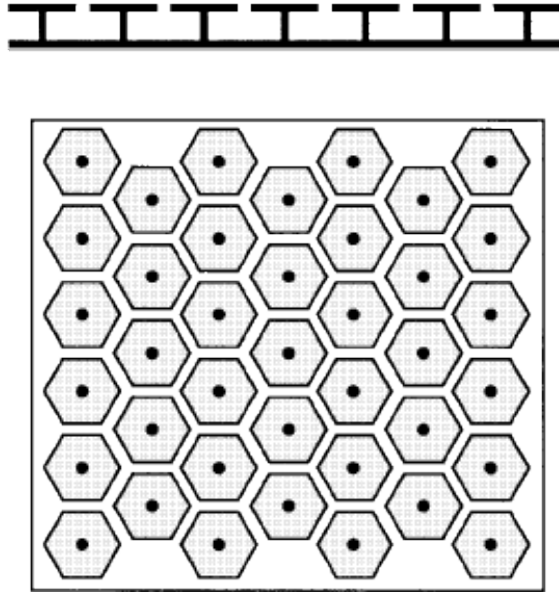
Figure 2.3: Mushroom-type EBG structure Source: [6]

Chiral Metamaterials

An object is chiral if it lacks geometrical symmetry (rotation or reflection). A chiral metamaterial is built from chiral material that has ability to rotate the plane of polarization of light. The refractive index depends on the chirality parameter κ:

$$n = \pm\sqrt{\varepsilon_r \mu_r} \pm \kappa.$$
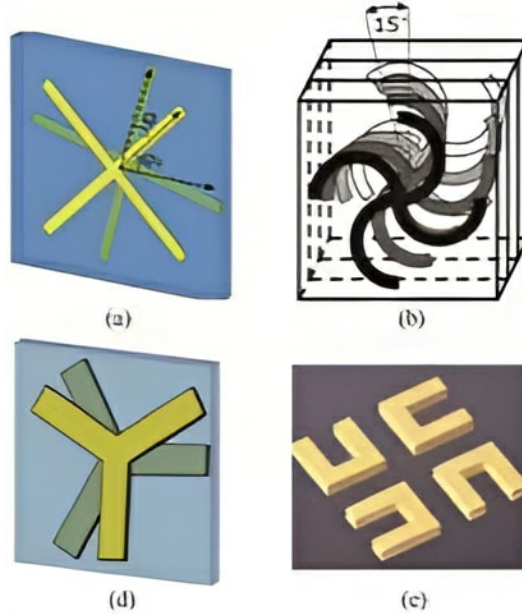
Figure 2.4: Different geometries of chiral metamaterials. Source: [7]

Terahertz Metamaterials

It operates in the terahertz range (0.1 to 10 THz), where ordinary materials show negligible magnetic response but metamaterials due to their negative values of permeability can exhibit tailored responses. The response depends on the geometry of the structure, which can be **tuned** by altering the dimensions or the geometry to achieve desired response.
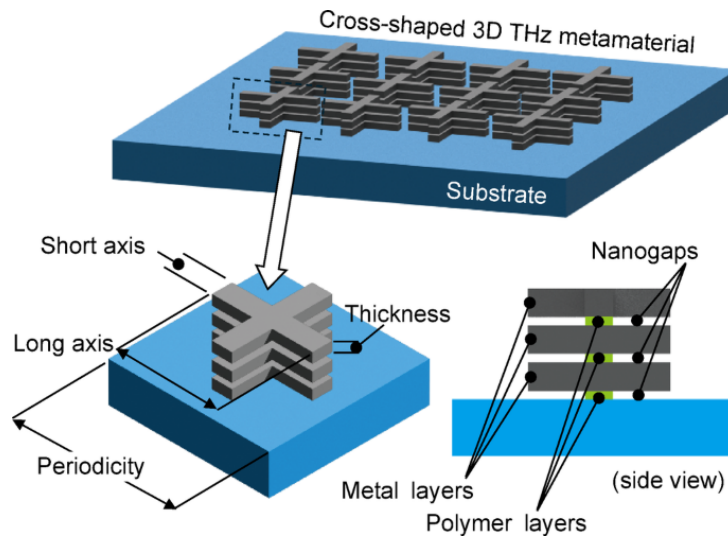
Figure 2.5: 3D THz metamaterial with vertical nanogaps. Source: [8]

Photonic Metamaterials

It operate at optical frequencies and derive their properties from the structure that is smaller than the interacting wavelength (sub wavelength), unlike photonic crystals, whose optical properties arise from Bragg scattering in a periodic lattice.

Tunable Metamaterials

Materials whose effective properties (e.g., refractive index or the resonant response) can be dynamically adjusted by external stimuli (electric, magnetic, thermal).

Frequency Selective Surface (FSS) based Metamaterials

FSS are engineered to selectively reflect, absorb, or transmit waves at specific frequencies. FSS can be composed of two-dimensional planar components in periodic arrays. High-Impedance Surfaces (also known as Artificial Magnetic Conductors) are a class of FSS metamaterials whose metallic patterning supports unique surface-wave currents and impedance characteristics.

Nonlinear Metamaterials

Metamaterials can be fabricated from the material which exhibit nonlinear response when their internal field strength exceeds the applied external field. The nonlinear constitutive relation is:

$$\vec{D} = \epsilon_1 \vec{E} + \epsilon_2 \vec{E}^2 + \epsilon_3 \vec{E}^3 + \dots$$

2.2 Applications

2.2.1 Metamaterial Absorbers

Metamaterial absorbers can be engineered to exhibit high absorbance either across a broad wavelength band, at a single designated frequency, or at multiple discrete frequencies. They are designed to have a near-unity absorption coefficient, meaning they can absorb almost all incident electromagnetic waves without reflection or transmission. Absorbance can be calculated using following relation:

$$A(\omega) = 1 - \left|S_{11}(\omega)\right|^2 - \left|S_{21}(\omega)\right|^2$$

where S_{11} and S_{21} are the reflection and transmission coefficients, respectively. When an electromagnetic wave is impinged on to the metamaterial surface, it can be scattered, reflected, or absorbed. The top surface of the metamaterial is made rough to suppress any type of scattering. Similarly, to minimize the transmittance (ideally 0) a metal plate is used as the bottom layer. This works, because electromagnetic radiations cannot pass through metals. Finally, reflectivity is minimized by matching the impedance of the metamaterial to that of free space. This is achieved by altering the dimension of material until effective permeability is equal to effective permittivity ($\mu_r = \epsilon_r$).

$$Z = Z_0\sqrt{\frac{\mu_0\mu_r}{\varepsilon_0\varepsilon_r}}, \quad Z_0 = \sqrt{\frac{\mu_0}{\varepsilon_0}} \approx 377 \ \Omega. \tag{2.1}$$

Apart from impedance matching, the article **Metamaterial Electromagnetic Wave Absorbers**, Watts, Liu, and Padilla (2012)(ω) [23] explains there are quite a few more phenomena such as resonance, plasmons, and nanoparticle gratings that can help us build a perfect absorber . Earlier, in resonance, a metal backing is placed at $\lambda/4$ spacing from the resistive sheet. In transmission line theory, this transforms the short circuit to an open circuit, creating a resonant condition, if the impedance of the resistive sheet matches that of free space.

Modern metamaterial absorbers, utilize a three-layer structure. The uppermost layer usually consists of an Electric Ring Resonator (ERR) along with the ground plane (bottom metal layer), which creates an electric response by coupling strongly to the incident electric field at a certain resonance frequency. The bottom metal layer is spaced apart from the middle layer by a dielectric and creates magnetic coupling via magnetic polaritons, which creates antiparallel currents in the cut wire and the center wire of the ERR. An incident time-varying magnetic field may couple to these antiparallel currents, thus yielding a Lorentz-like magnetic response. This layered configuration takes advantage of both electric and magnetic responses. If instead of an ERR, a cavity-like structure is used, then the structure will exhibit cavity resonance, where the electromagnetic waves get trapped within a specific geometry via multiple reflections.[23]
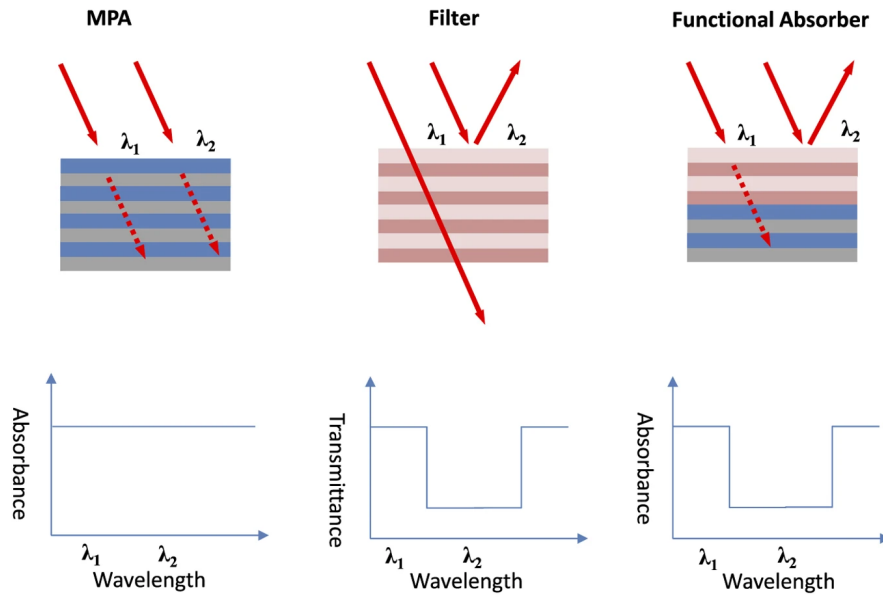
Figure 2.6: Evolution from broadband to spectrally-selective absorption: (left) Metamaterial Perfect Absorber (MPA) absorbs all wavelengths λ_1 and λ_2, (center) dielectric filter selectively transmits λ_1 while reflecting λ_2, (right) functional absorber integrates both components to achieve wavelength-selective absorption—absorbing λ_1 while rejecting λ_2. Source: [9]

2.2.2 Superlens

All positive focal length lenses and optical devices have the ability to converge light. However, beyond a certain focal length (the diffraction limit), refractive power cannot reduce the minimum focal spot size producing a blurry image .

Most telescopes, microscopes, cameras and other lens have a circular aperture. Light is diffracted when it is passed through the circular aperture, forming **Airy Disk**, a bright

central spot with concentric rings as depicted in fig 2.6. Any two objects (or light sources) closer than the size of the Airy disk cannot be resolved. Unresolved objects creates **evanescent waves**, which are exponentially decaying waves that carry information about the object. These carry subtle information about the shape of the object. Since they are exponentially decaying, they cannot be captured by a lens with a positive focal length.
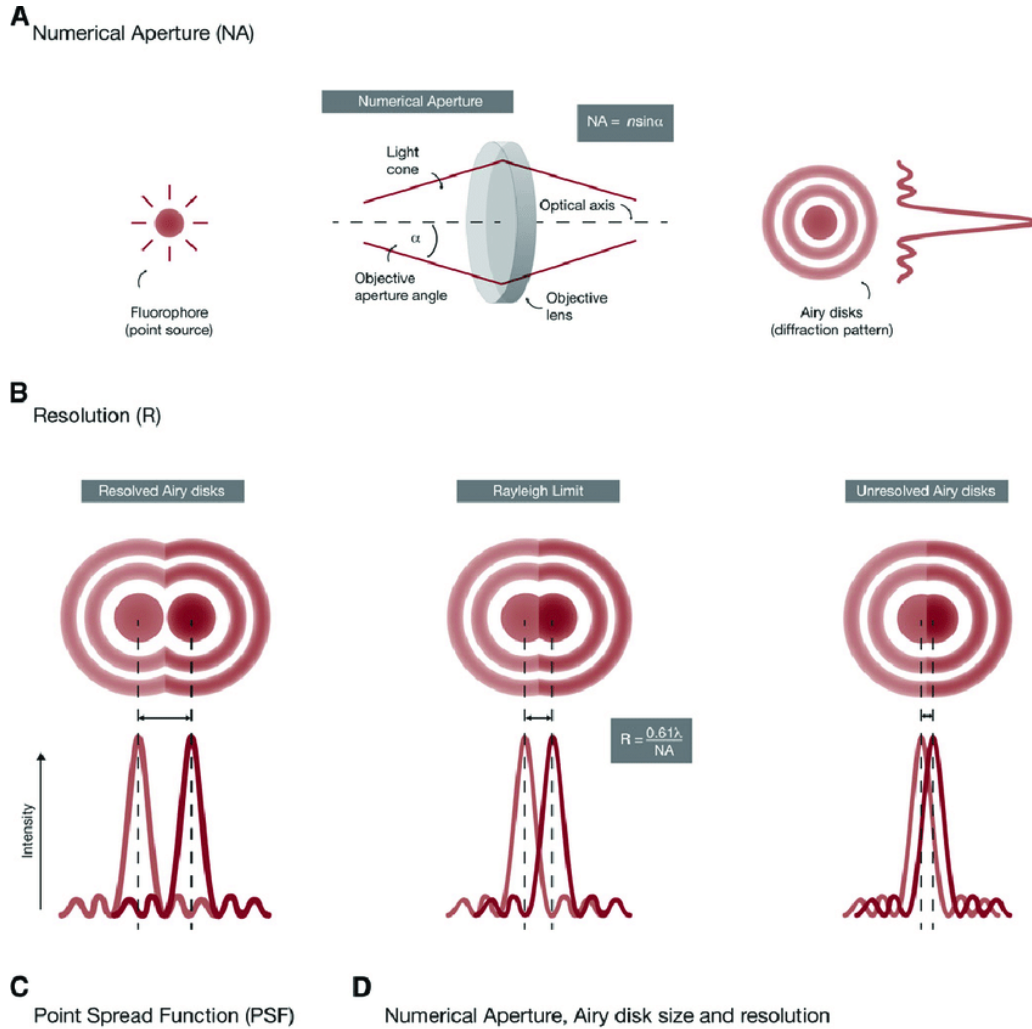
Figure 2.7: Relationship between numerical aperture, diffraction-limited resolution, and the Rayleigh criterion showing resolved, critically resolved, and unresolved Airy disk patterns with corresponding intensity profiles. Source: [10]

However, a **superlens** which is just a lens made from metamaterial can recover these evanescent waves and focus them to form an image with resolution beyond the diffraction limit. This is because metamaterials have negative refractive index, which allows them to bend light in the opposite direction compared to conventional materials.
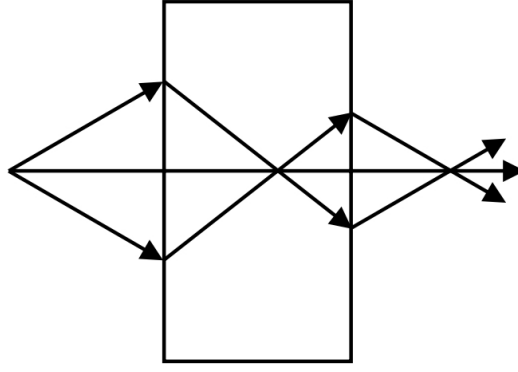
Figure 2.8: Superlens converging light beyond the diffraction limit. Source: [1]

2.2.3 Cloaking Device

Theoretical designs use wave bending around objects to render them invisible without distortion.

This is can by accomplished by two methods:

1. **Bending Waves:** Metamaterials can alter the path of electromagnetic waves by artificially controlling the speed and direction of light using negative refractive index metamaterials which has the ability to bend the light backwards and by using graded index material which can slow the speed of the wave.

2. **Scattering Cancellation:** We can also coat the object with a metamaterial that can generate waves in backward direction, which will then cancel out the natural scattering of the object. This is known as scattering cancellation.
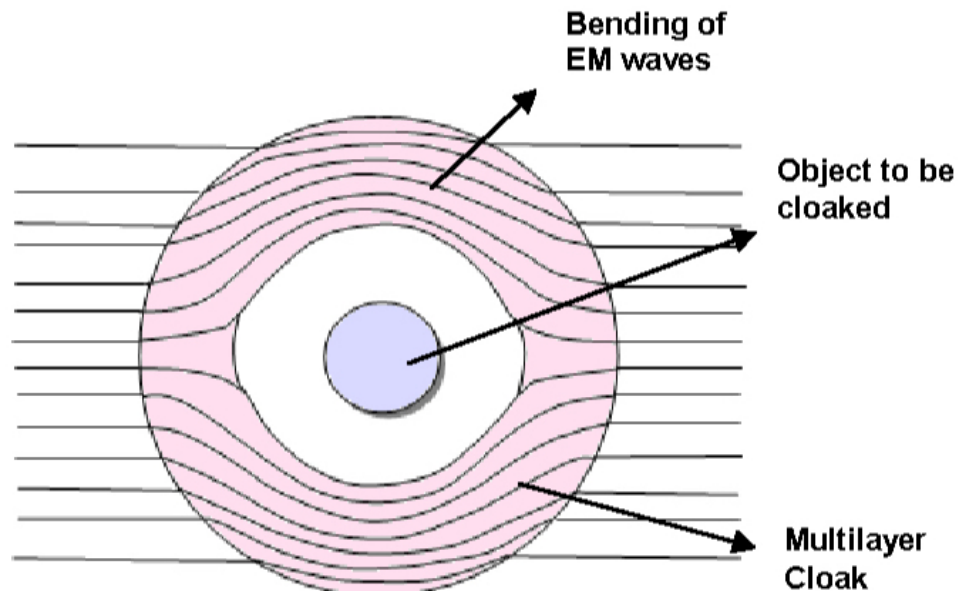
Figure 2.9: Conceptual cloaking device. Source: [11]

2.2.4 Antennas

Another key area where metamaterials are employed is in the design and engineering of antennas. Their unique features, such as their periodic structure, high directivity, and electromagnetic band-gaps, help in storing and radiating energy while also drastically reducing the antenna size, mimicking the performance characteristics of larger antennas. They overcome conventional limitations by reducing signal reflection, increasing the bandwidth and the gain of the antenna. There are 4 key types of different antennas:

1. **Zero-Phase-Shift:** These antennas uses uniform magnetic field to transmit ultra high radio frequency or WLAN signals without changing their phase.

2. **Gap-Capacitor:** This type of antenna, arranges itself in a way which creates a L-band radar resonance (ZOR) using a narrow capacitive gap, allowing compact, efficient radar operation.

3. **Mushroom Cells:** As the name suggests, these antennas are designed in the shape of a mushroom that enhances WIFI signals by controlling how wave spreads.

4. **High-Permittivity Dipoles:** They are made up of high-permittivity materials to create compact dipole antennas that can operate at lower frequencies. Due to their compact size, they are used in multiple input multiple output (MIMO) cellular towers.

Other applications include seismic protection and sound filtering.
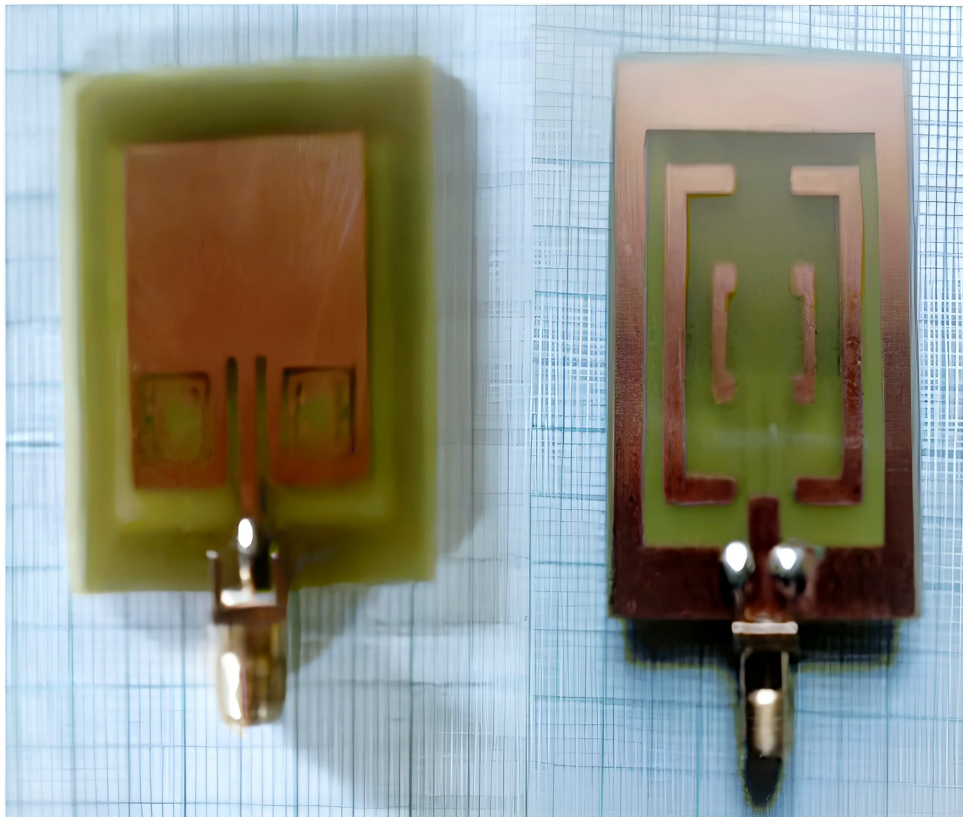
Figure 2.10: Front and back side of a fabricated metamaterial-based rectangular patch antenna designed on FR4 for 2.4 GHz WiFi applications. Source: [12]

Chapter 3

LITERATURE REVIEW

In the previous chapter, subsection 2.2.1, general formation mechanism of metamaterials absorbers was discussed. which were impedance matching, transmission line theory and the using a metal layer to minimize transmission (reflection theory). However, for a broadband metamaterial, these mechanisms alone are not sufficient. It along with other mechanism work collectively to create a broader absorption band. In this chapter, a review of various broadband metamaterial absorbers is presented.

3.1 Broadband Metamaterial Absorbers Mechanisms

3.1.1 Superposition of Resonance Peaks

This is one of the simples method to create a broadband metamaterial absorber. The idea is to put together different geometry together such that multiple resonance peaks are superimposed to create a broad absorption band.
In song *et al.* (2018),[13] merged two different geometry, each with a single resonant peak to create a dual-band absorber.
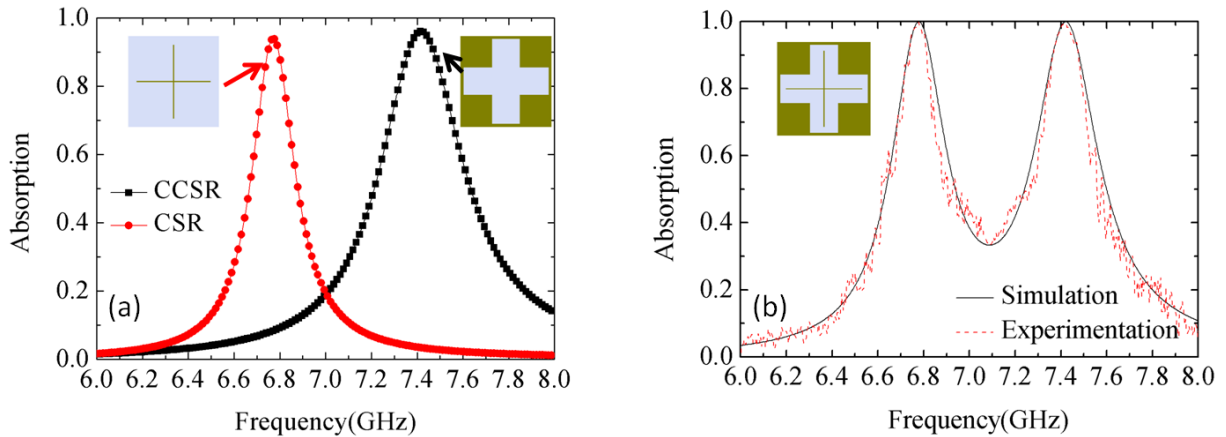
Figure 3.1: Geometry and the absorption performance of each design (left) and the combined geometry and it's dual band absorption curve (right). Source: [13]

Another instance where this method was used is in Hamza *et al.*, (2024), where a triple band absorber was creating by 4 different geometries, each with a single resonant peak.
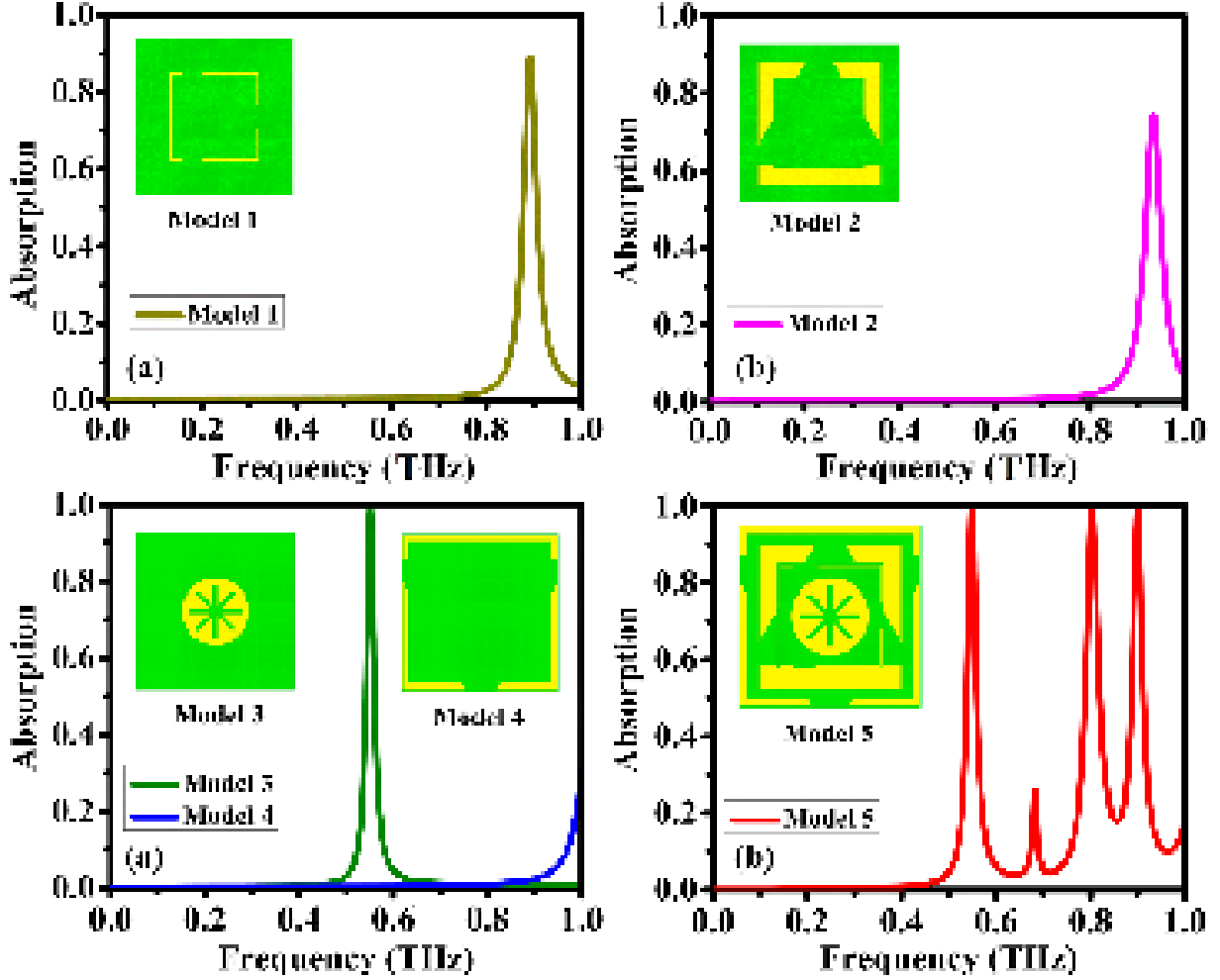
Figure 3.2: Geometry and the absorption performance of each design (model 1, model 2, model 3 and model 4) and the combined geometry (model 5) and it's triple band absorption curve. Source: [14]

This method is simple but it is important to keep in mind that the individual peaks shouldn't destructively superimpose each other. This can negatively impact the absorption performance of the combined geometry. In our proposed structure, which is discussed in the next chapter, this same method is used to create a broadband absorber.

3.1.2 Resonance phenomena

It comprises of 3 main phenomena:

- **Magnetic resonance:** In this phenomena, magnetic field induces circulating currents in the surface. The most common way to achieve is to introduce closed loop geometries in your absorber which will naturally induce circular current effectively creating an effective magnetic dipole. The most common shape used to achieve this is the split ring resonator (SRR). The SRR is a closed loop geometry with a gap in it which allows the magnetic field to induce a circulating current. The induced current creates a magnetic dipole which interacts with the incident electromagnetic wave, leading to absorption. Figure 3.1 shows a SRR based metamaterial absorber along with circular currents from H.-L. Huang *et al.*(2017) [24].

16
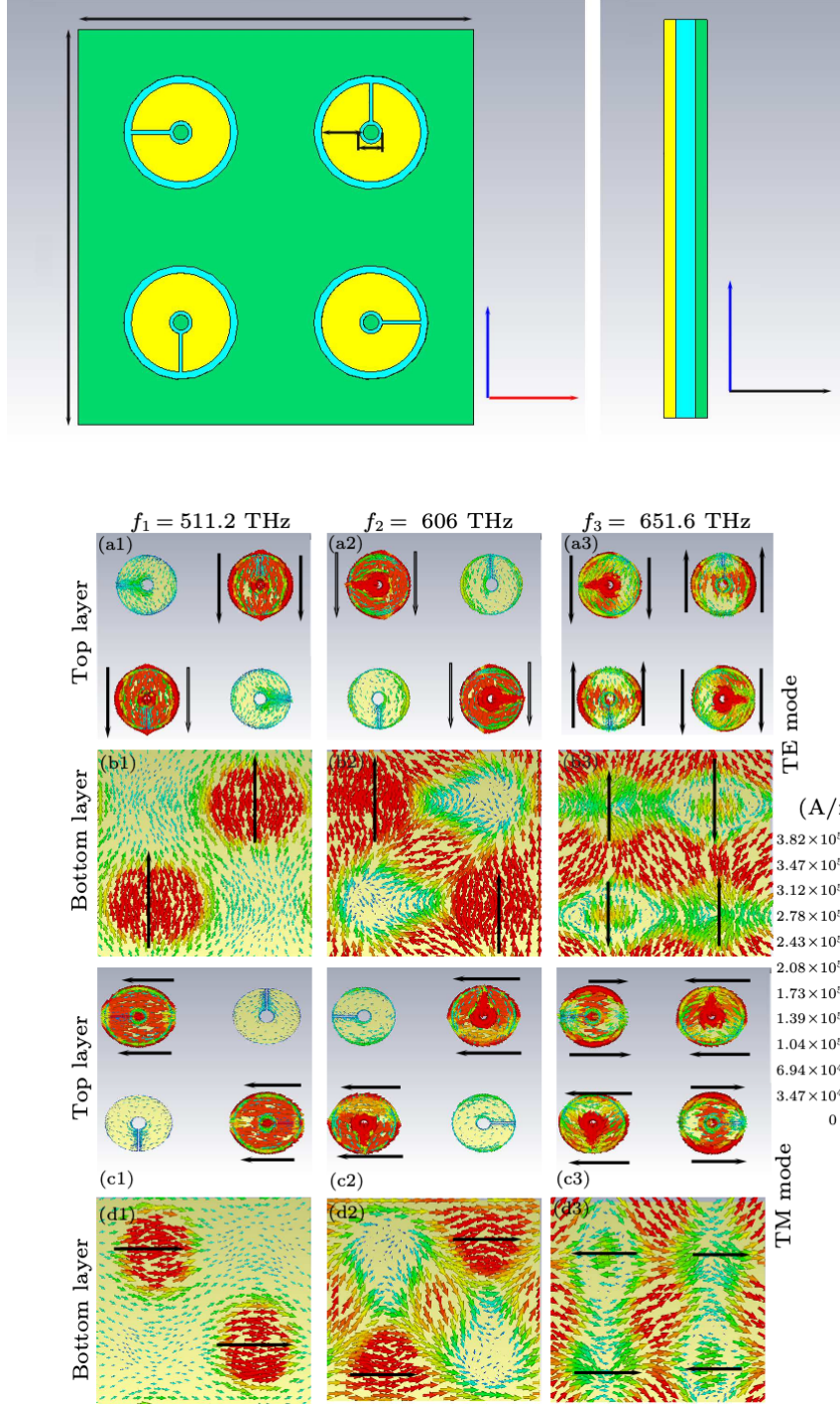
Figure 3.3: SRR geometry showing the existence of magnetic resonance due to circular surface currents. Source [15]

- **Electric resonance:** This phenomena is majorly due to plasmonic effects which occur at the metal dielectric surface. Plasmons are electric dipoles which get excited by the electric field component of the incident electromagnetic wave., resulting in a resonant response. Despite, in many metamaterials, plasmonic effects is a major factor which contribute to a high absorption performance electric resonance can occur in can occur in systems without free electrons, such as dielectrics, molecules, or specific structural designs , where resonant interaction of the electric field takes

place with bound electrons. In plasmonic effects surface plasmon polaritons (SPP) and localized surface plasmons (LSP) are the most common electric resonance phenomena. Surface plasmon polaritons involve coupling between the electric field and electron plasma oscillations at a metal-dielectric interface Similarly, localized surface plasmons in nanoparticles result from the electric field inducing electron oscillations, leading to absorption through ohmic losses. A surface plasmon is characterized by a electric field hotspot which propogates along the metal dielectric surface while a LSP is characterized by an electric field hotspot which is concentrated in nanoparticles. Figure 3.3, shows a Ultra-broadband metamaterial absorber from Qi *et al.* (2019) [16] is shown where the SPRs was used to achieve a broadband absorption performance and the figure 3.4 shows a triband metamaterial absorbers where LSPs dominate.
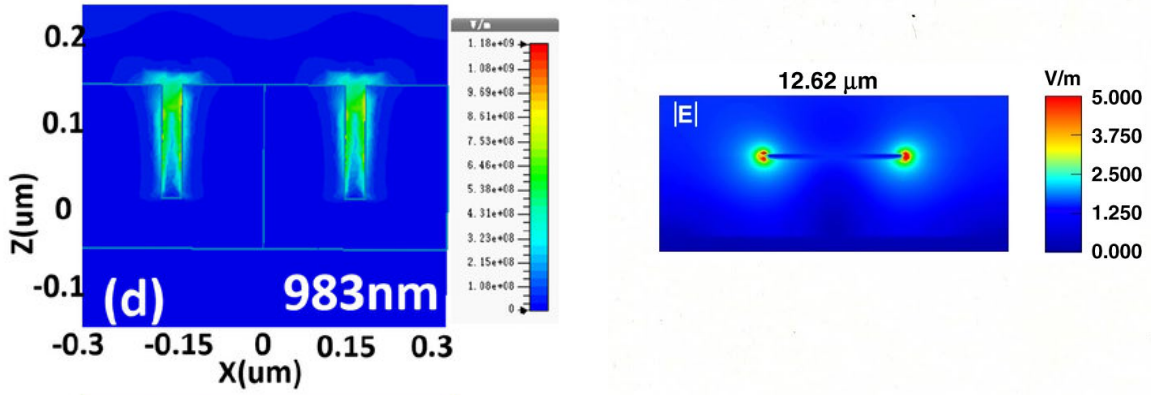
Figure 3.4: Comparison of SPP (left) and LSP (right) based metamaterial absorber geometries and their absorption performance (triple-band curves). Source: [15] [16]

- **Magntic Polariton (MP) :** This is a similar phenomena to magnetic resonance. The MPs are hybrid quasiparticles formed by the strong coupling of photons with magnetic dipole oscillations in metamaterials. To detect the presence of MPs, electrical field vectors should circulate around the dielectric to form current loops, which induces the diamagnetic response and eventually excite MPs. In figure a MP based metamaterial absorber from Cai *et al.* (2025) is shown where arrows indicate electric field vectors forming circular loops. However, in Yang Bai *et al.*(2015), the same concept is shown presented differently. It indirectly shows MPs by showing opposite phases of electric field at a metal-dielectric-metal surface. The top metal induced a positive charge , while the bottom metal induce a negative induced charge. The opposite happens in the other half of the cycle. Finally, the opposite surface charge oscillations creates a current loop through the dielectric spacer and back through the metals.
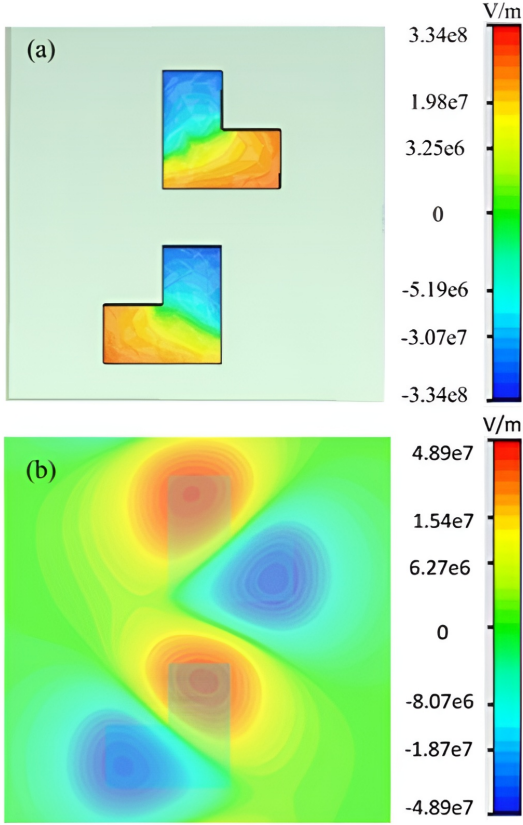
(a) Opposite sign of electric of field in the two metal surfaces of the metamaterial hinting existence of magnetic polaritons. Source: [25]
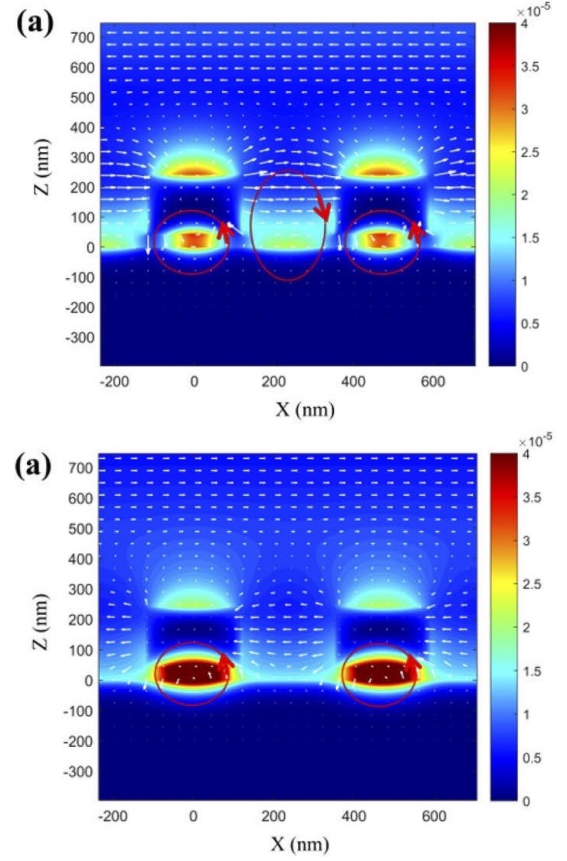
(b) Metamaterial absorber showing the presence of magnetic polaritons by the presence of circular electric field vectors. Source: [26]

3.1.3 Material Composition and Structural Configuration

The material composition and structural configuration indirectly determine the absorption mechanism. They themselves don't create a new mechanism but they play a major role in influencing what mechanism will dominate the absorption performance.

1. **Material Composition:** The choice of materials of metamaterial absorbers determine the type of application they will be suited for. According to Faisal *et al.* (2024) [27] demonstrated that highly conductive metals , such as gold and silver, are broadly used for their plasmonic properties. They have a relatively low ohmic losses compared to other metals which is why they are used in building biosensors. The main disadvantage of using gold and silver is that both are expensive which makes cost production high. Also, silver oxidizes easily, so to prevent this a protective layer is applied onto it's surface which suppress it's performance. Aluminum is sometimes used as a substitute for gold and silver because of it's low cost but it has much weaker performance as mentioned by Jia *et al.* (2022) in the journal paper A Simple Metamaterial for High-Performance Spectrum-Selective Absorption in the Visible Region.[28] Other metals such as titanium and nickel which is probed by Zhou *et al.* (2021) [15] have high

thermal stability and a large imaginary part permittivity makes it suitable for applications in stealth and thermophotovoltaics. Similarly, dielectrics can also be classified on the basis of the mechanism of absorption you want to achieve. For example, Wu *et al.* (2023) [29] illustrated low loss dielectrics, such as silicon dioxide (SiO$_2$) and silicon nitride (Si$_3$N$_4$), are often used for achieving high absorption by impedance matching and cavity resonance, while Xu *et al.*(2021) in his journal paper Broadband Solar Absorber Based on Square Ring Cross Arrays of ZnS [30] concluded,high indexed dielectrics such as zinc selenide (ZnS) is used to shift resonance wavelengths.

2. **Structural Configuration:**

   For quantifying the absorption performance a dimensionless quantity called quality factor (Q-factor) is used. It represents the ratio of resonant frequency to the full width at half maximum (FWHM) and describes the relationship between the resonance bandwidth and its center frequency according to a theoretical equation.

   $$Q = \frac{f_0}{\Delta f}$$

   Here f_0 represents the centeral frequency of the resonant peak and Δf represents the frequency interval between FWHM. A lower value of Q-factor indicates a good absorber. Since, most metamaterials absorbers can be modeled to an equivalent to a LCR circuit, we can equate their Q-factor. In an LCR circuit, we define the Q-factor as:

   $$Q = \frac{1}{R}\sqrt{\frac{L}{C}}$$

   Here, R represents the equivalent resistance of the absorber, L is the equivalent inductance of the of the absorber, and C represents the equivalent capacitance.

   The three parameters (R, L, and C) now can be tweaked that will affect the absorption to achieve broadband absorption response. For example, in the paper by Rajni *et al.* (2016) [17], the authors used a SRR geometry where the inductance (L) corresponds to metal traces/rings which acts as current loops, capacitance (C) corresponds to the gaps between metal elements that help in storing electric energy and resistance (R) corresponds to ohmic losses in metals, dielectric losses in substrates and in the metal dielectric metal metamaterial absorber bottom metal plate represents the inductor, the top metal patches and the dielectric spacer represents the capacitor and the total losses in the absorbers represents the resistance.
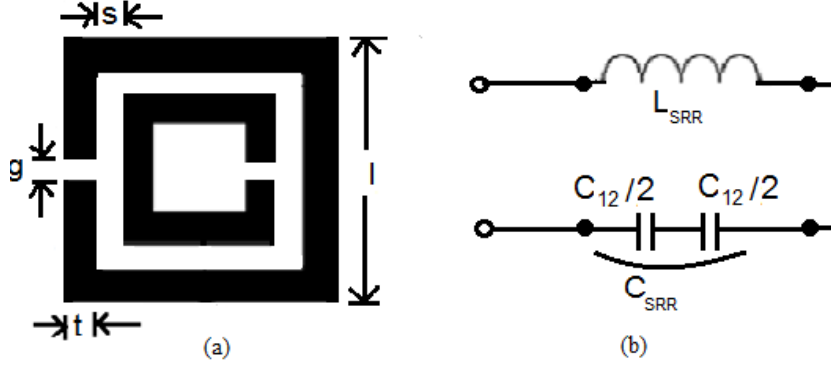
Figure 3.6: Equivalent circuit model of a SRR metamaterial absorber. Source: [17]

In a broadband metamaterial absorber often multiple mechanism work together to achieve a broadband absorption performance.

3.2 Wide-Angle, Polarization-Independent Dual-Band Infrared Absorber: L-Shaped Metamaterial

Review by Yang Bai *et al.*

[25] In this section, a brief review of paper is presented which discusses geometry, mechanism and the shortcomings. Our work is an extension of this work, where we create a broadband absorber.

In this paper, the authors proposed a metal dielectric metal double L shaped dual-band metamaterial absorber.

The author first designed a single L shaped metamaterial absorber as shown in figure 3.7.
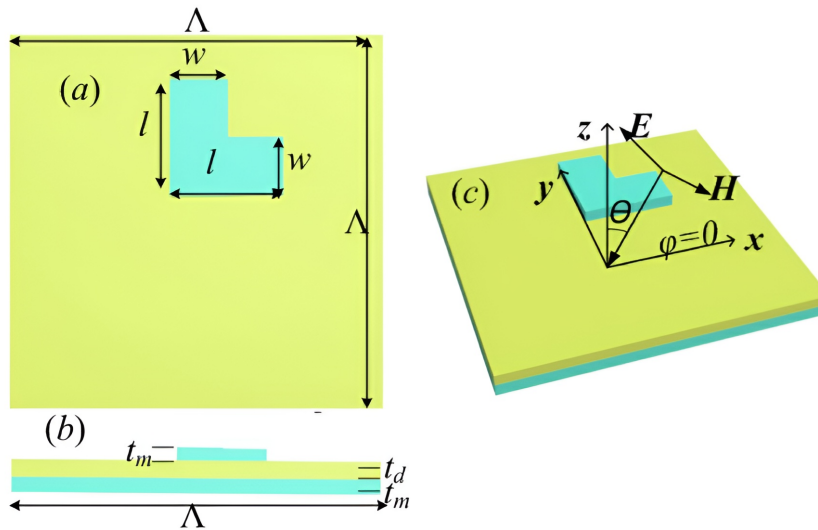
Figure 3.7: Single L-shaped metamaterial absorber geometry and the absorption performance for TE and TM modes.

However, in the TE case, it's absorption performance dipped when θ was varied becuase mangetic polaritons weren't effectively excited.
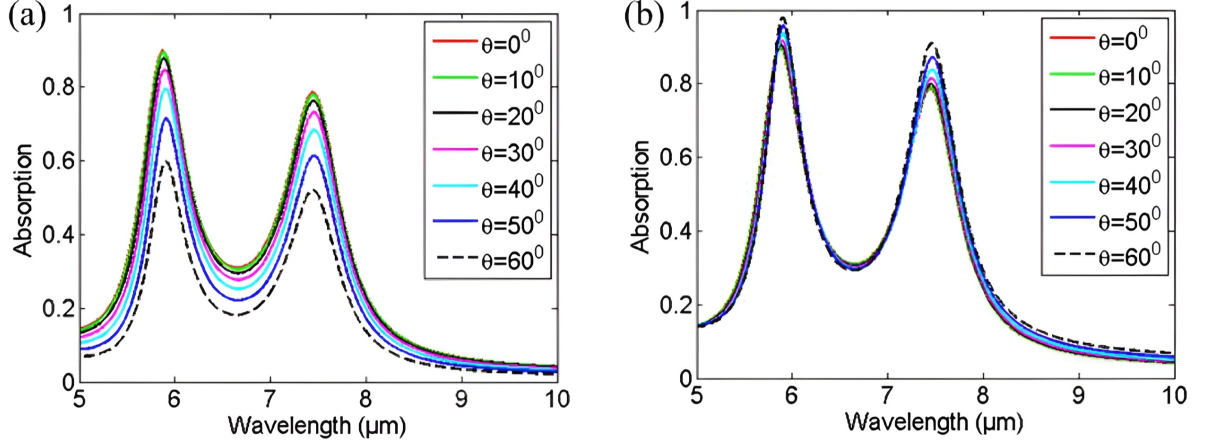
Figure 3.8: TE mode (left) shows reduced stability at $\phi = 60°$; TM mode (right) shows stability for all ϕ.

The author modified the single L structure by a doubly L structure.
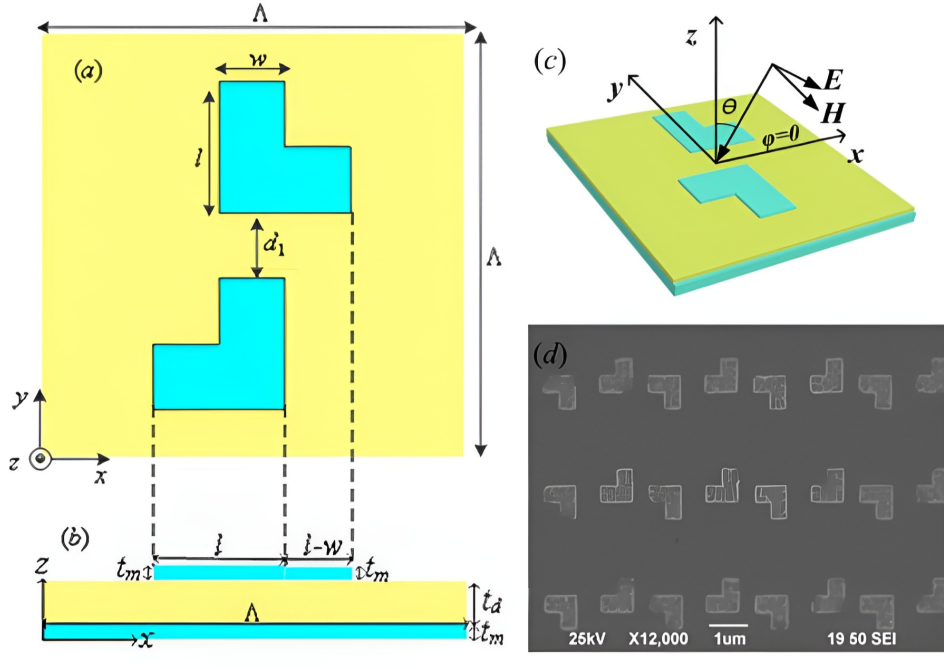
Figure 3.9: (a) Top view, (b) Side view, (c) Light incidence on the L-shaped metamaterial, (d) SEM image of the fabricated L-shaped absorber.

Here, t_m, t_d represent the thickness of metal and dielectric, respectively. The substrate is silica carbide (SiC) and the bottom layer and L-shaped patches are made of gold, modeled by the Drude model for dielectric function.

Results

The absorption spectra along with real and imaginary parts of impedance were plotted.
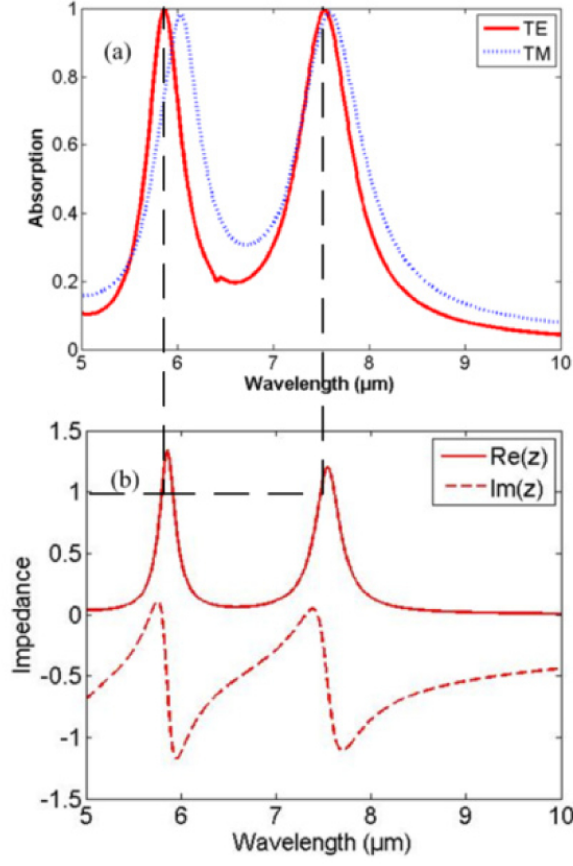
Figure 3.10: Absorption spectra and impedance for TE and TM modes at $\theta = 45°$ and $\phi = 0°$.

Then the stability of the absorber was tested by varying the angle of incidence θ and azimuthal angle ϕ. in both TE and TM modes.
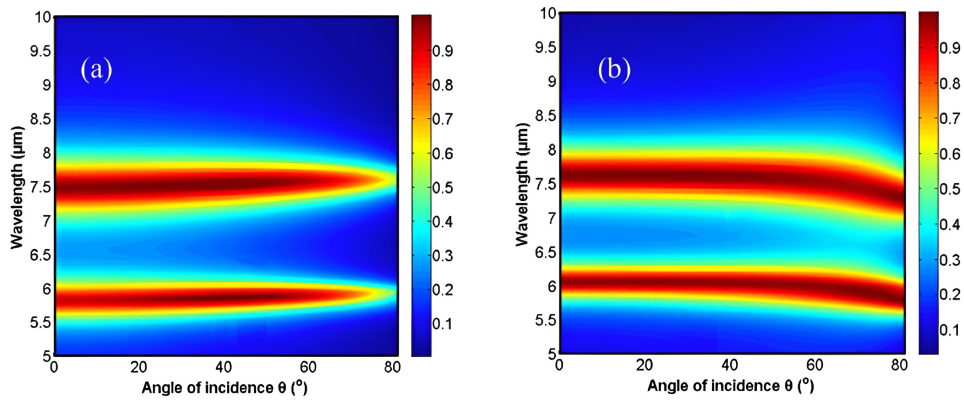
Figure 3.11: Electric field distribution for TE mode (left) and TM mode (right) for varying θ at $\phi = 45°$.
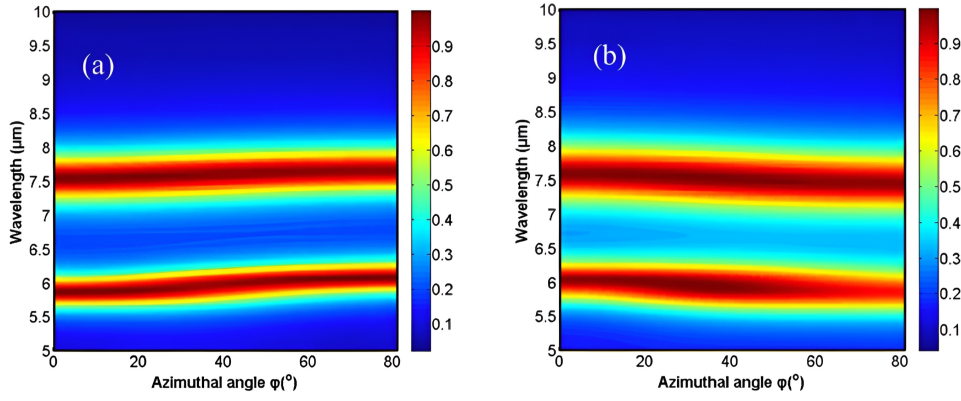
Figure 3.12: Electric field distribution for TE mode (left) and TM mode (right) for varying ϕ at $\theta = 0°$.

As shown in the figures 3.11 and 3.12, with the new double L structure the structure were polarize insensitive at the resonant peaks.

To understand the mechanisms behind it, the z component of electric field at both metal interfaces for both resonant wavelength were plotted.
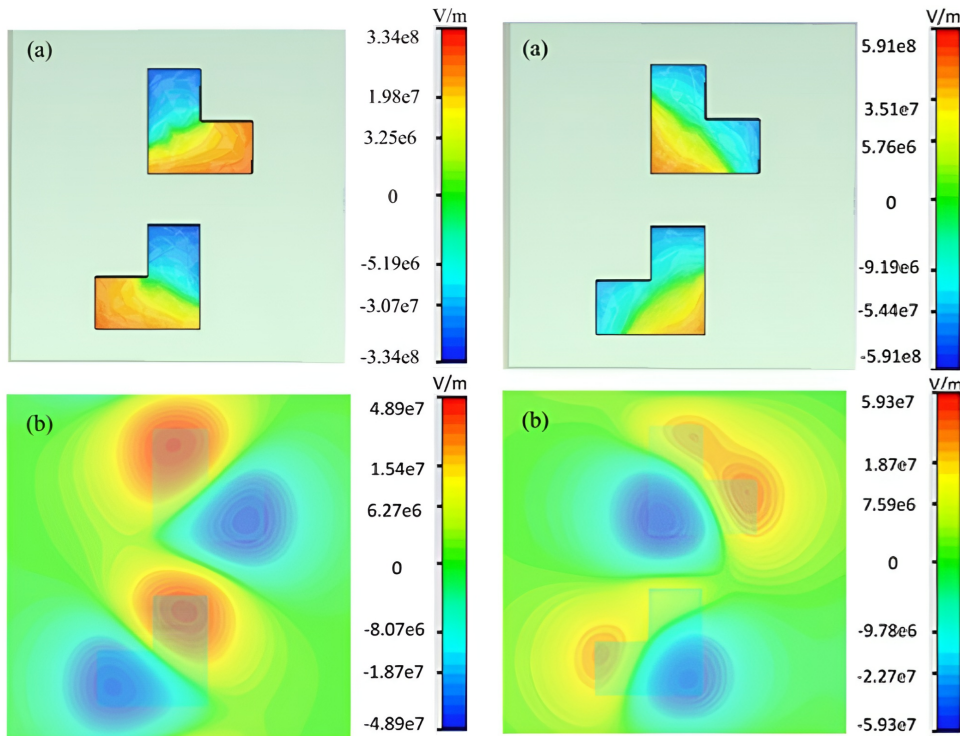
(a) Electric field distribution at $\lambda = 7.5\,\mu$m   (b) Electric field distribution at $\lambda = 5.86\,\mu$m

Figure 3.13: Opposite phases of the electric field at the two metal interfaces for the two resonant wavelengths confirms the existence of magnetic polaritons.

Finally, an equivalent LCR circuit model was proposed to explain the absorption performance of the double L structure.
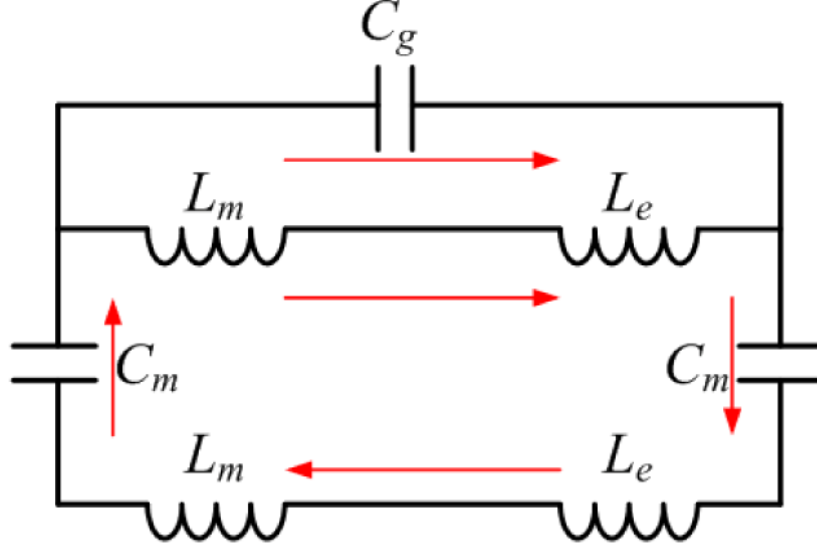
Figure 3.14: Equivalent LCR circuit model for the double L-shaped metamaterial absorber.

The key **advantages** of this design were it was such simple yet effective design. It showed near perfection absorption performance at both TE and TM modes and was also polarize insensitive. The major **disadvantage** of the proposed structure was that it was a dual band absorber, so it is only suited for niche applications and not much suited for practical applications. Also, the thickness of gold used was high (100 nm) which makes the manufacturing cost high making production at scale difficult.

Chapter 4

ABSORBER GEOMETRY AND MODELING

4.1 Comsol Multiphysics

First to learn the basics of Comsol Yang Bai *et al.* work's was replicated and simulatedA.1. Comsol Multiphysics is a simulation software that help us simulate various physical phenomena such as electrodynamics , heat transfer , fluid dynamics.

It has a built in CAD (Computer-Aided Design) module that allow us to create a model from scratch and also allow us to perform advanced numerical calculations on our model .

Then in the next step the initial designs of metamaterial absorber were created and simulated which are shown in A.2 in the appendix.

The starting point for the proposed structure was a design inspired by Yang Bai *et al.* [25]. As mentioned in the previous chapter, despite its drawback, this design significantly improves its bandwidth while maintaining near unity performance.

4.2 Metamaterial Absorber Design

Figure 4.1 and 4.2 illustrates the schematic of the top-down view of proposed design of the metamaterial absorber. Each geometric entity was meticulously introduced to enhance the overall absorption efficiency of the material via an iterative procedure. The figure 4.3 shows the side view of the unit cell, and it demonstrates that the unit cell is a tri-layer metal - dielectric - metal(MDM) configuration. Gold layers (basal and geometric entities) are shown in yellow color. The intermediate dielectric layer is made from silicon carbide (SiC), shown in grey color. The colors used in the diagram are not true to the actual color of the material.
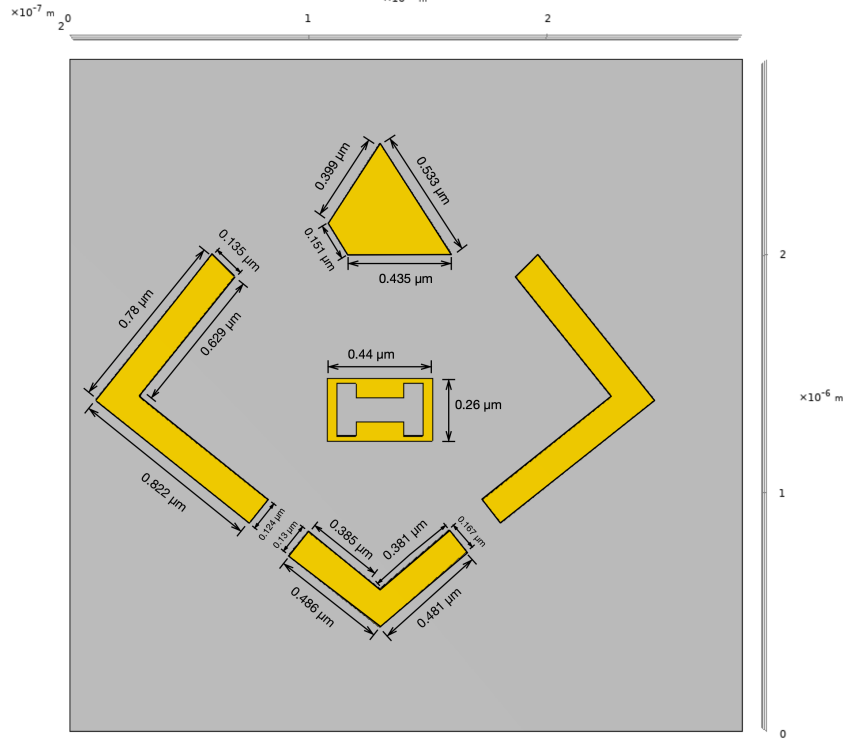
Figure 4.1: Top-view schematic of the metamaterial unit cell showing the geometric parameters with their dimensions. The structure consists of an outer triangular element, L-shaped arms, and central H-shaped cavity on the top gold layer.
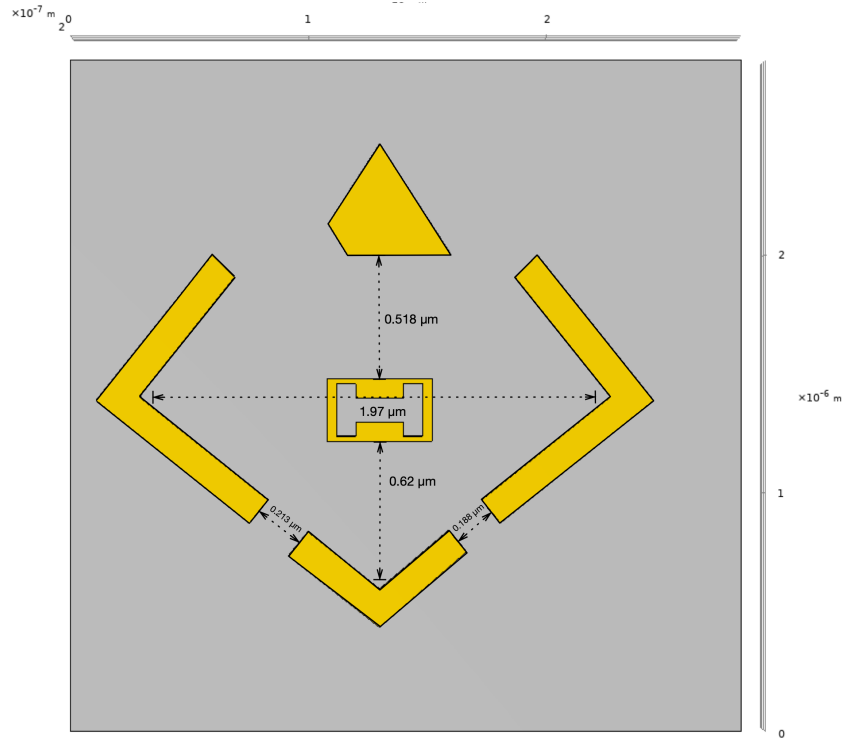

Figure 4.2: Top-view schematic of the metamaterial unit cell showing spatial relationships between metamaterial components.

Despite its high cost, gold is the preferred choice as the metal for many metamaterials because it exhibit surface plasmon resonance (SPR)[31] phenomena where its electron undergo collective when specific wavelength of light is incident making it ideal for plasmonic applications especially in the infrared regime. To characterize its optical response we have adopted the Drude-Lorentz model for metals, where the dielectric function is given by:[32]

$$\epsilon(\omega) = 1 - \frac{\omega_{p,D}^2}{\omega^2 - i\omega\,\gamma_D} + \frac{F\,\omega_{p,L}^2}{\omega_0^2 - \omega^2 + i\omega\,\gamma_L} \quad 1$$

$\omega_{p,D} = 1.2 \times 10^{16}$ rad/s is the plasma frequency for the Drude (free-electron) term.[25]
$\gamma_D = 10.5 \times 10^{13}$ rad/s is the damping (collision) frequency for the Drude term.[25]
$\omega_{p,L} = \omega_{p,D}$ is the plasma frequency associated with the Lorentz (resonant) term.
$\omega_0 = 0$ is the resonance frequency of the Lorentz oscillator
$\gamma_L = \gamma_D$ is the damping coefficient for the Lorentz resonance.
$F = 1$ is the oscillator strength factor for the Lorentz term.

The choice of SiC as the dielectric spacer was due to its relatively high refractive index[33] and high absorptive losses[34] within the mid-infrared range, so that it could improve the metamaterial's general performance properties. The value of the dielectric constant ϵ for SiC is taken to be 10.8 and with a loss tangent dissipation factor $\tan\delta$ equal to 0.003.[25]

The thicknesses of each gold layer (t_m) and the dielectric layer (t_d) are $0.05\mu m$ and $0.27\mu m$ respectively. The thickness is chosen to be such that it minimizes the cost of production by enabling utilization of fabrication techniques like Nanoimprint Lithography instead of more precise fabrication techniques such as Electron Beam Lithography (EBL), which is not only exponentially more expensive but also more time consuming making it less suitable for production at scale. The thickness is large enough that it ensures structural robustness ensuring it is not too fragile while also minimizing the material consumption, lowering cost of material consumptions relative to other already existing designs which have a thickness greater than $0.6\mu m$.
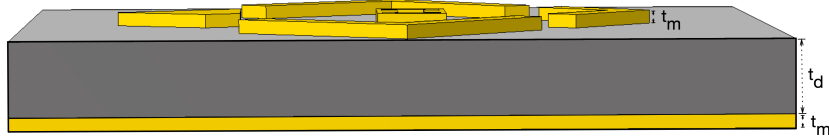
Figure 4.3: Side-view schematic of the Metal-Dielectric-Metal (MDM) metamaterial absorber showing layer thicknesses. Gold layers (yellow) with thickness $t_m = 0.05$ μm sandwich the SiC dielectric layer (grey) with thickness $t_d = 0.27$ μm.

The numerical simulation was performed in Comsol Multiphysics© v6.1 in the Electromagnetic Waves, Frequency Domain module. Floquet-Bloch periodic conditions are used in $\vec{x}$ and $\vec{y}$ directions to produce infinite arrays of unit cells. This condition

---

[1]This Drude-Lorentz model will effectively reduce to Drude model for metal.

enforces a phase change relation, requiring that the solution on one boundary equals that on the opposite boundary multiplied by a complex phase. This factor makes it ideal for modeling wave propagation in periodic media. The formula for the phase change relation can be written as:[35]

$$E(\vec{r} + \vec{a}) = E(\vec{r})e^{i\vec{k}\cdot\vec{a}}$$

Here:

$E(\vec{r})$: Electric field at position $\vec{r}$
$\vec{a}$: Lattice vector (translation vector in the periodic structure)
$\vec{k}$: Wavevector
$e^{i\vec{k}\cdot\vec{a}}$: Complex phase factor imposed by the periodic boundary condition

A Perfectly Matched Layer (PML) is also implemented atop the structure to absorb outgoing radiations that could inflate absorption values.[36] The thickness of it is set to $0.44\mu m$ with scaling factor equal to $1/\cos\theta$. Pardiso solver was chosen since it excels at providing robust calculations.[37] A quadratic discretization scheme and a fine mesh with refinement for conductive edges were employed so that there is a good balance of accuracy, while keeping the load on processor optimal and calculations do not take excessive time. An excitation port was set up parallel to X-Z plane to impinge metamaterial structure with transverse component of electric field at an incident angle ($\phi = 0°$) and elevation angle $\theta = 45°$.
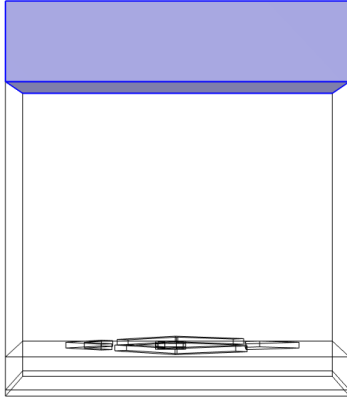
(a) Implementation of the Perfectly Matched Layer (PML) in the COMSOL simulation with thickness $0.44\,\mu$m and scaling factor $1/\cos\theta$. The PML absorbs outgoing radiation to prevent artificial inflation of absorption values due to boundary reflections.
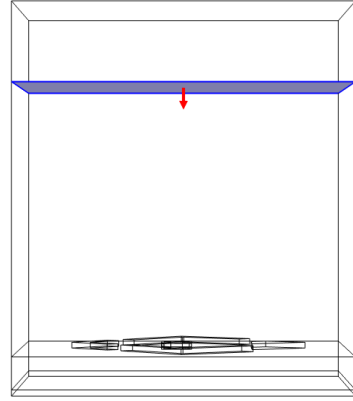
(b) Excitation port configuration parallel to the X–Z plane used to impinge the metamaterial structure with the transverse component of the electric field at azimuthal angle $\phi = 0°$ and elevation angle $\theta = 45°$. The port enables precise control of electromagnetic wave parameters for performance evaluation.

Finally a parametric sweep is computed for the range $3.3 - 4.4\mu m$ with a step size $= 3.33 \times 10^{-8}m$ to find the spectral dependance of absorption ($S21$) and reflection coefficient (S11 in db scale) using the formula:

$$A(\lambda) = 1 - S11$$

Chapter 5

RESULTS and DISCUSSION

Figure 5.1 (a) and (b) shows the absorption spectrum (S_{21} parameter) and the reflection coefficient (S_{11} in dB scale) at $\phi = 0°$ and $\theta = 45°$. It was observed that the structure was able to achieve average absorption over 98% with a bandwidth of $0.7\mu m$ $(3.4 - 4.1\mu m)$ in the TE mode. The peak absorbance achieved in this bandwidth was $\approx 99.99\%$ at $\lambda \approx 3.932\mu m$. The broadband nature of the absorber is quantified using the effective quality factor via resonance bandwidth from the absorption graph:

$$Q_{\text{eff}} \;=\; \frac{\lambda_0}{\Delta\lambda} \;=\; \frac{3.75\,\mu\text{m}}{0.7\,\mu\text{m}} \;=\; 5.36 \tag{5.1}$$

where $\lambda_0 = \frac{3.4+4.1}{2} = 3.75\,\mu$m is the central wavelength of the absorption band and $\Delta\lambda$ is the bandwidth of the absorption spectrum which is equal to $4.1\,\mu$m $- 3.4\,\mu$m $= 0.7\,\mu$m. This low Q-factor confirms efficient wideband operation, critical for applications such as thermal imaging and radiative cooling.
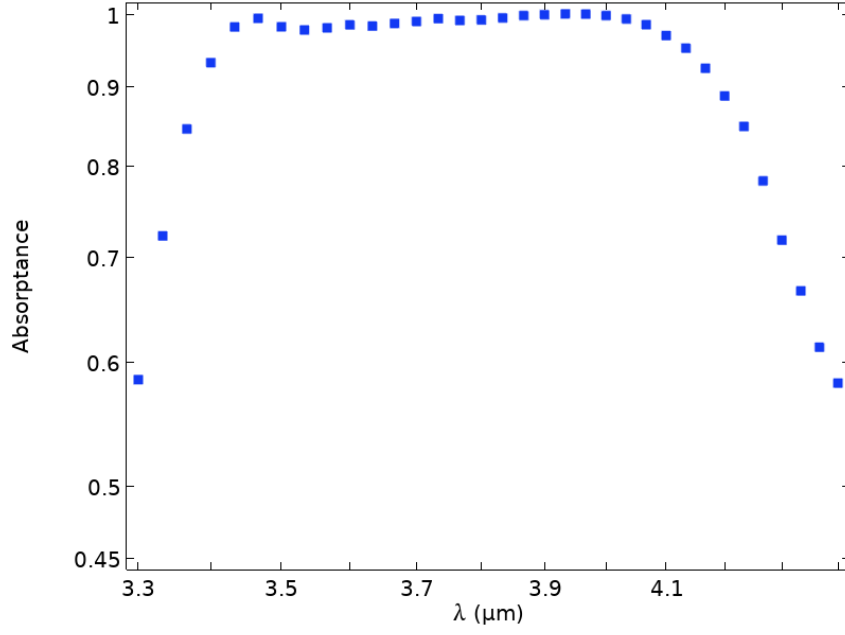
(a) Absorption spectrum of the metamaterial structure showing over 98% average absorption at incident angles $\phi = 0°$ and $\theta = 45°$.
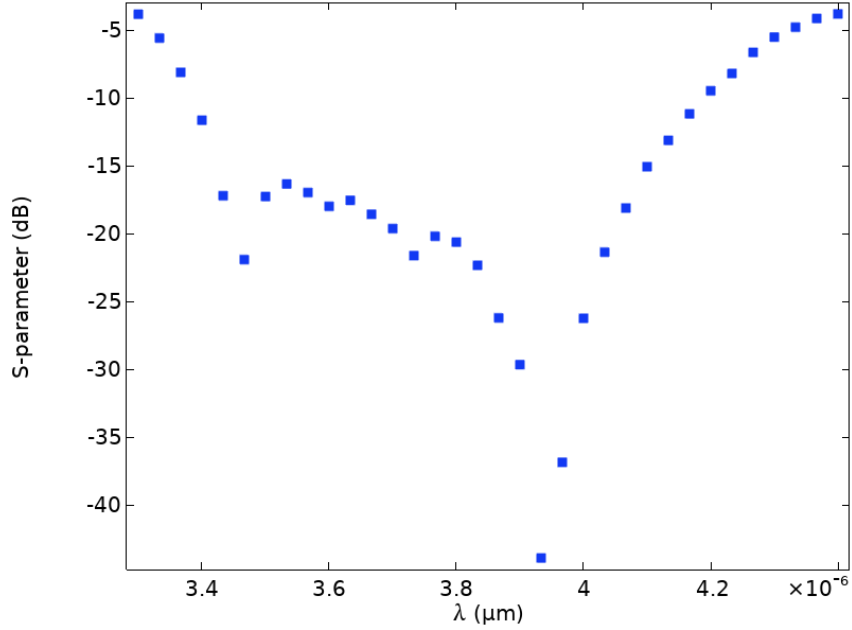
(b) Reflection coefficient (S_{11}) spectrum in dB scale at $\phi = 0°$ and $\theta = 45°$.

Figure 5.1: (a) Absorption spectrum and (b) Reflection coefficient spectrum of the metamaterial absorber, both measured at $\phi = 0°$ and $\theta = 45°$.

5.0.1 Resonance Mechanisms and Field Localization

To investigate the underlying mechanisms behind the high absorption, electromagnetic field distributions were analyzed. The exceptional absorption performance arises from a hybrid resonance mechanism rather than one dominant resonance.

Figure 5.2 (a) and (b) shows colormaps of $\vec{E}_Z$ of the top and bottom metal layers at resonance wavelength of $3.932 \mu m$. The top and bottom layers exhibited opposite signs hinting the presence of magnetic polaritons. The opposite polarity pattern in the top layer and bottom layer indicated the presence of magnetic resonance.
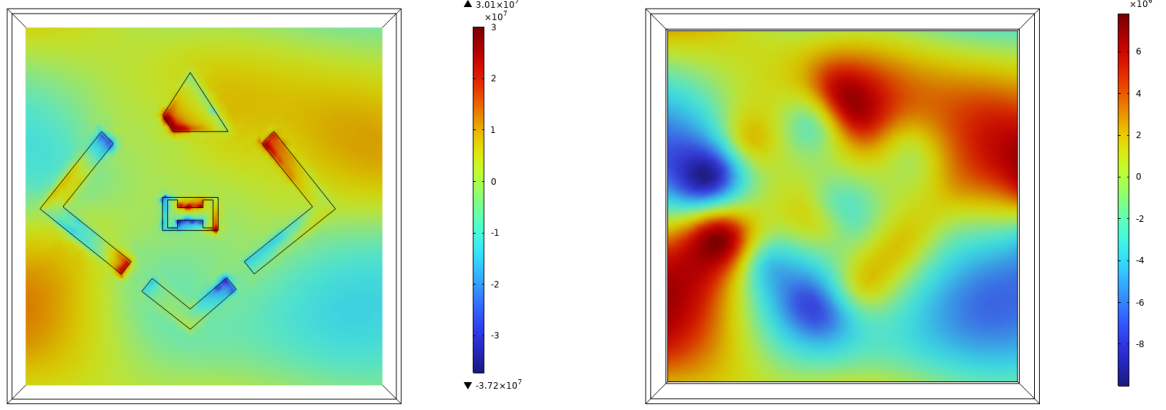
(a) Electric field distribution (Ez) in the top gold layer at $\lambda = 3.932 \, \mu$m.

(b) Electric field distribution (Ez) in the bottom gold layer at $\lambda = 3.932 \, \mu$m.

Figure 5.2: Electric field distribution (Ez) (a) in the top gold layer and (b) in the bottom gold layer at resonance wavelength ($\lambda = 3.932 \, \mu$m).

To confirm this conclusively, Fig.4 presents an arrow plot of volume current density (J) and the magnetic field (H). The current in the individual elements was linear however collectively current forms a circular loop. Similarly, the magnetic field also forms circular vortex. Both of these results are a hallmark of the magnetic polaritons.
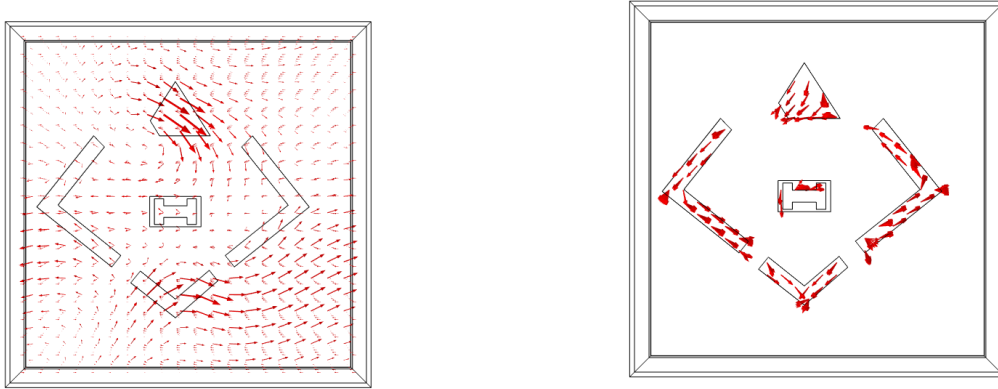
(a) Magnetic field (H) at resonance wavelength ($\lambda = 3.932 \, \mu$m).

(b) Current arrow plot at resonance wavelength ($\lambda = 3.932 \, \mu$m).

Figure 5.3: (a) Magnetic field (H) and (b) Current arrow plot at resonance wavelength ($\lambda = 3.932 \, \mu$m) showing circular loop and vortex that confirm the presence of magnetic polaritons contributing to the absorber's high performance.

Additionally, we investigated the localized surface plasmon (LSP) contribution by analyzing electromagnetic hotspots in the top metal layer. Fig 7 shows the plot of

$|\vec{E}|$ at resonance wavelength of $3.932\mu m$ revealing localized hotspots predominantly at the edges and corners of our metallic structure, particularly at the triangle corners, L-shaped boundaries, and H-shaped cavity regions. This field localization pattern is the characteristic signature of LSPs, confirming their significant contribution to the absorption mechanism through electromagnetic energy concentration at sub wavelength scales. By confirming LSPs, surface plasmon polaritons (SPP) mediated effects can be conclusively ruled out as the dominant mechanism which are propagating electromagnetic modes bound to the metal dielectric interface with evanescent decay perpendicular to that interface.
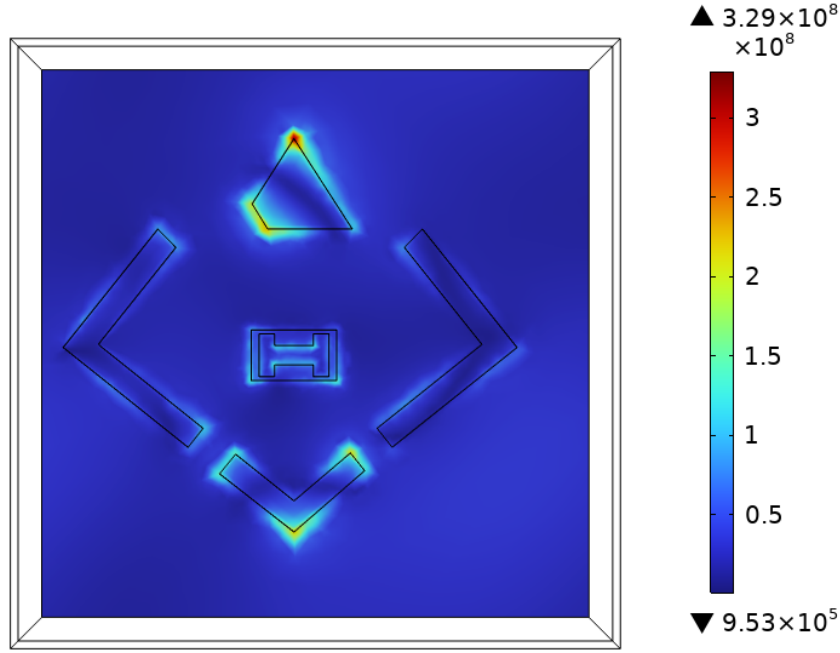
Figure 5.4: Electric field magnitude ($|\vec{E}|$) at resonance wavelength ($\lambda = 3.932\,\mu$m) showing localized hotspots at edges and corners of the metal structure, confirming the presence of LSPs.

5.0.2   Power Dissipation and Loss Mechanisms

The COMSOL variable Q_h represents the volumetric power dissipation density (in W/m³) arising from both ohmic and dielectric losses in an electromagnetic simulation. Mathematically, it is represented by :

$$Q_h \;=\; \underbrace{\tfrac{1}{2}\,\sigma\,|\mathbf{E}|^2}_{\text{Ohmic loss}} \;+\; \underbrace{\tfrac{1}{2}\,\omega\,\varepsilon_0\,\varepsilon''\,|\mathbf{E}|^2}_{\text{Dielectric loss}} \tag{5.2}$$

A volume integration of the same was computed across the metal and dielectric layers to quantitative analyze power dissipation, which revealed that 89.1% of total losses (14.5 W) occur in the metallic layers, compared to 10.9% (1.79 W) in the dielectric spacer. This 8.9:1 ratio confirms that ohmic losses dominate the absorption mechanism, consistent with plasmonic systems. The physical reason associated with

high ohmic losses is primarily due to complex permittivity which encodes electron scattering losses in metals. The minimal dielectric contribution ensures broadband performance by avoiding narrowband resonance damping. Fig. 5.5 qualitatively quantify the power dissipation by plotting the Q_h in the metal and dielectric layers.
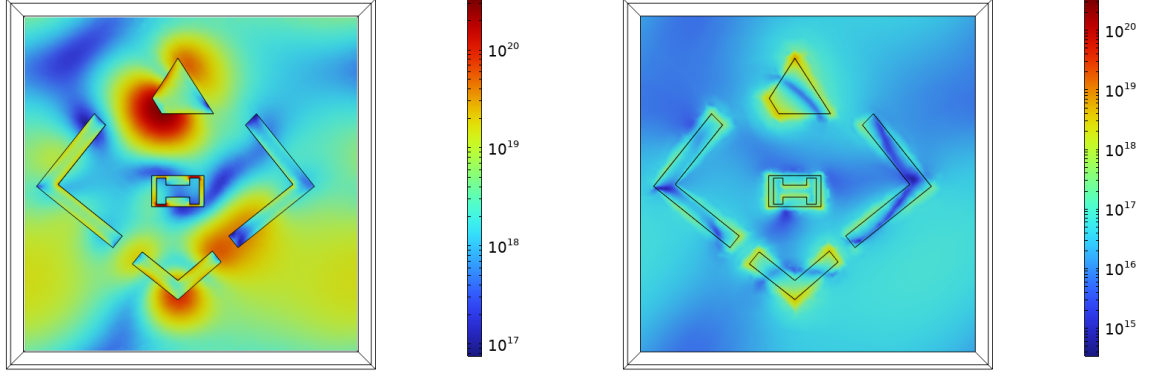
(a) Power dissipation density in the metal layer showing dominant ohmic losses.

(b) Power dissipation density in the dielectric layer with lower losses.

Figure 5.5: Power dissipation density in (a) metal layer showing dominant ohmic losses, and (b) dielectric layer with lower losses.

5.0.3 Impedance Matching and Eigenfrequency Analysis

Real and imaginary parts of impedance (Z) of the structure were calculated and plotted in Fig. 5.6 for the same wavelength range using the following relations:

$$Z_{real} = Re\left(\frac{1+S11}{1-S11}\right), Z_{imag} = Im\left(\frac{1+S11}{1-S11}\right)$$

It can be seen the real part of impedance (Z_{real}) $\approx 1 - 1.2$ while imaginary part (Z_{imag}) is oscillating btw ± 0.2, which is close to 0. . This near-unity real impedance with negligible imaginary component demonstrates excellent impedance matching to free space ($Z_o = 1$), further enhancing absorption.
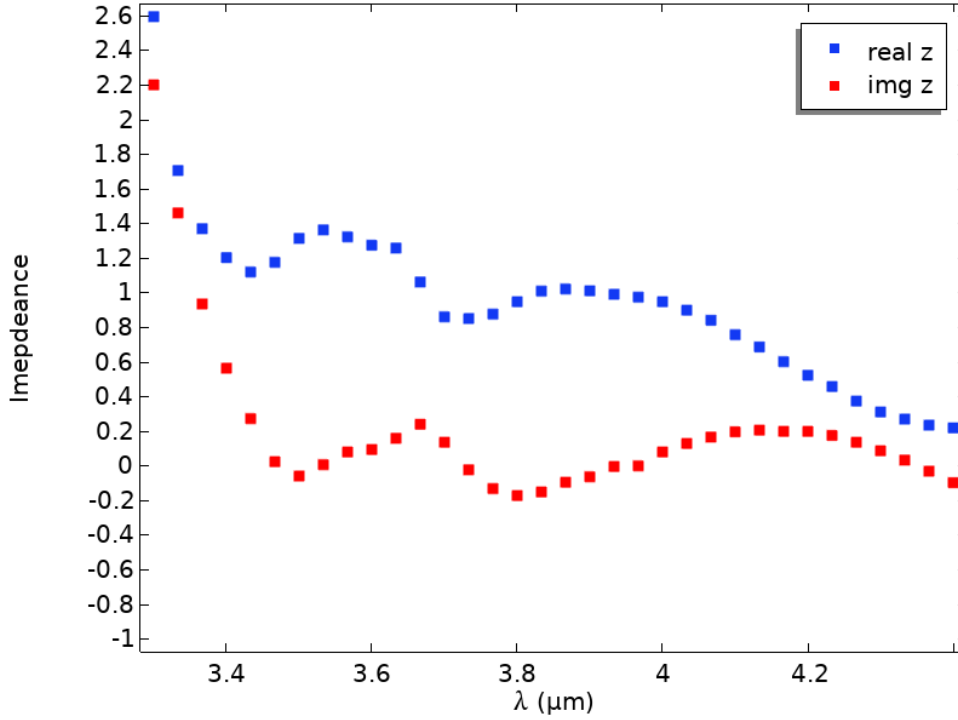
Figure 5.6: Real and imaginary parts of normalized impedance (Z) across the operating wavelength range.

Additionally, an Eigenfrequency analysis was performed in COMSOL Multiphysics to determine the natural resonant modes of our structure. In an absorbing resonant system, the eigenfrequency are complex values complex and can be expressed as $\omega = \omega' + i\omega''$ where ω' is the real part and ω'' is the imaginary part. It quantifies the the damping rate of an oscillator by calculating quality factor (Q). It is calculated using the following relation:

$$Q = \frac{\omega'}{2\,|\omega''|} \tag{5.3}$$

The higher-Q modes (Q ¿ 10) likely contribute to specific spectral features but have less impact on the overall broadband response. Table 1 represent the eigenfrequency, frequency, and the corresponding quality factor of the structure. A few For example, the eigenfrequency at 72.902 THz has an imaginary component of 6.089 THz, yielding:

$$Q_{73.169\,\text{THz}} = \frac{72.902\,\text{THz}}{2 \times 6.0.89\,\text{THz}} = \frac{72.902}{12.178} = 5.9857 \tag{5.4}$$

Similarly,for the 82.326 THz mode with an imaginary component of 9.169 THz:

$$Q_{82.326\,\text{THz}} = \frac{82.326\,\text{THz}}{2 \times 9.169\,\text{THz}} = \frac{82.326}{13.6204} = 4.4892 \tag{5.5}$$

The results reveal multiple resonant modes within our operating band (3.4-4.1 μm), with Q-factors ranging from 4.48 to 38.3. This close correlation between the absorption-derived Q-factor (5.36) and the eigenfrequency analysis Q-factors (5.9 and 4.4) confirms that these low-Q modes are the dominant contributors to the broadband absorption behavior.

35

Table 5.1: Eigenfrequencies, Frequencies, and Quality Factors

Eigenfrequency (THz)	Frequency (THz)	Quality factor (1)
66.608+1.4454i	66.608	23.041
71.047+4.3745i	71.047	8.1206
72.902+6.0897i	72.902	5.9857
74.699+2.7434i	74.699	13.614
76.896+1.2444i	76.896	30.897
78.096+1.2928i	78.096	30.204
81.389+1.1169i	81.389	36.437
82.326+9.1694i	82.326	4.4892
83.982+1.2523i	83.982	33.532
85.325+1.2481i	85.325	34.183
85.713+1.1194i	85.713	38.287
87.187+2.6780i	87.187	16.278

## 5.0.4 Angular Stability Analysis

We assessed the angular stability of our structure by presenting a 2 dimensional heat map of the absorption spectrum for different elevation angles θ (Fig 5.7 (a)) and incident angle ϕ (Fig 5.7 (b)). Figure number 5.7 shows majority of the graph is dominated by the red and orange color indicating high absorption for majority of elevation angles θ. The peak absorption is represented by dark red absorbed across 3 separate wavelength ranges from 3.3 to 3.5 μm for $\theta = 35°$ to 50° , 3.55 to 3.7 μm for $\theta = 45°$ to 62° and 3.85 to 4.0 μm for $\theta = 35°$ to 60°. The absorption performance dips for small elevation angles ($\theta = 0°$ to 25°) except for 3 small patches specially the one which spans across 3.85 to 3.95 μm wavelength range. Similarly, the absorption performance starts dips for large elevation angles ($\theta = 70°$ to 90°) which is shown in yellow green color. The absorption performance is also stable for incident angles (ϕ) up to 45°. The high absorption shows a parabola profile. In particular, at $\lambda = 3.33\,\mu m$, the absorption shows a consistent high performance reaching maximum at $\phi = 35°$. As wavelength increases stability increases with maximum stability achieved in centre ($\lambda = 3.85\mu m$), where the high absorption is stable upto $\phi = 45°$. On the further increasing the wavelength, the stability diminishes, returning to a maximum stable angle of $\phi = 35°$ at $\lambda = 4.10,\mu$m. Absorption performance degrades at high angles ($\theta > 50°$) except in the middle region, wavelength range of $3.75 - 4.0\mu m$ where the proposed structure still shows high absorption upto $\phi = 75°$.

Table 5.2: Elevation-angle (θ) Dependence of Absorption

θ range	Absorption level	Wavelength band(s) (µm)	Notes
0°–25°	Low (dips)	—	Except small patches at 3.85–3.95
35°–50°	High (peak)	3.30–3.50	Dark-red hotspots
45°–62°	High (peak)	3.55–3.70	Dark-red hotspots
35°–60°	High (peak)	3.85–4.00	Dark-red hotspots
70°–90°	Low (dips)	—	Yellow-green regions
> 50°	Mixed (mostly low)	3.75–4.00	High absorption up to $\phi = 75°$ in mid-bar

Table 5.3: Incident-angle (ϕ) Stability of High Absorption

λ (µm)	Stable ϕ range	Peak ϕ	Notes
3.33	up to 35°	35°	Monotonic rise, maximum at 35°
3.85	up to 45°	45°	Broadest angular stability
4.10	up to 35°	35°	Stability diminishes beyond this point
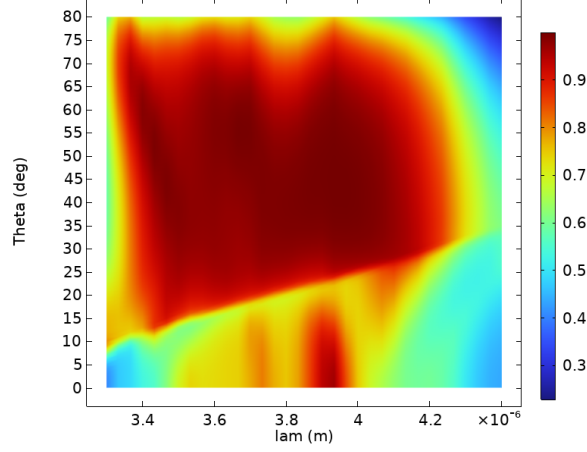
(a) Absorption spectra for different elevation angles (θ) at fixed incident angle ($\phi = 0°$).
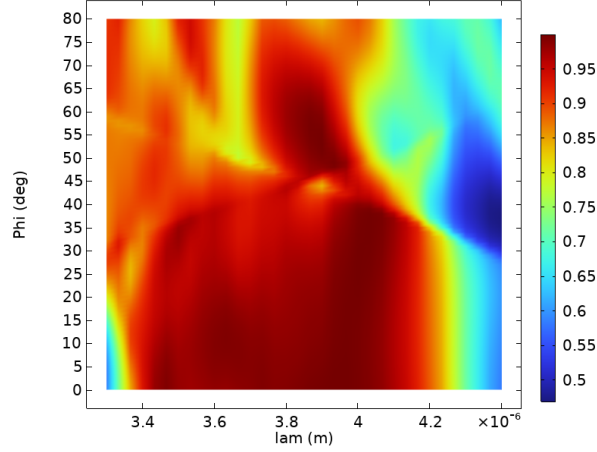
(b) Absorption spectra for different incident angles (ϕ) at fixed elevation angle ($\theta = 45°$).

Figure 5.7: Absorption spectra of the metamaterial absorber for (a) different elevation angles (θ) at fixed incident angle ($\phi = 0°$) and (b) different incident angles (ϕ) at fixed elevation angle ($\theta = 45°$).

Chapter 6

CONCLUSION AND FUTURE SCOPE

In this paper, a metamaterial structure is designed and simulated with novel geometry that is simpler complex geometry like fractal designs. The top metal layer comprises of an outer frame formed by a triangle at the top with a cut on the bottom left corner, an L-shaped boundary on the sides and bottom, and a central rectangle with an H-shaped cavity. The structure was able to achieve over 98% average absorption across a $0.7\,\mu$m bandwidth in the mid-infrared region (3.4–4.1 μm) with a peak absorption of $\approx 99.99\%$ at $\lambda \approx 3.932\,\mu$m. The primary reasons for high absorption were impedance matching, existence of magnetic polaritons and presence of localized surface plasmons (LSPs) at structural hotspots such as triangle corners and H-cavity edges. The absorber also demonstrated decent angular-dependent absorption characteristics, maintaining over 90% absorption in the 3.4–4.1 μm wavelength range for incident angles (ϕ) up to 40° and elevation angles (θ) from 30° to 65°. However, the performance degraded for incident angles $> 40°$ and extreme elevation angles. Eigenfrequency analysis further confirmed the dominance of low-Q resonant modes in sustaining broadband response, while power dissipation studies revealed that over 89% of the absorption losses originated from ohmic dissipation in metallic layers, consistent with plasmonic behavior. The high absorption efficiency, broadband response, and angular stability make the proposed absorber highly suitable for applications such as thermal emission and infrared detection systems. The proposed design also addresses practical implementation challenges by utilizing fabrication-friendly dimensions and efficient material usage, making it a significant step toward real-world metamaterial absorber applications. Furthermore, the proposed structure bridges the performance gap between narrowband and ultra broadband metamaterial absorbers by achieving average absorption while maintaining a moderate bandwidth. As mentioned in the introduction, this work is currently limited to numerical design and simulation; experimental validation is beyond its scope and will be pursued in future work.

Bibliography

[1] J. B. Pendry, "Negative refraction," *Contemporary Physics*, vol. 45, no. 3, pp. 191–202, 2004.

[2] A. Ali, A. Mitra, and B. Aïssa, "Metamaterials and metasurfaces: A review from the perspectives of materials, mechanisms and advanced metadevices," *Nanomaterials*, vol. 12, no. 6, p. 1027, 2022.

[3] EMPossible, "Lecture 13 (em21) – metamaterials," Online lecture slides, 2025, figure from EMPossible, accessed May 29, 2025. [Online]. Available: https://empossible.example.com/lectures/EM21/Lecture13

[4] J. Peatross and M. Ware, *Physics of Light and Optics*. Provo, UT: Brigham Young University, Department of Physics and Astronomy, 2010, available online: https://optics.byu.edu/docs/opticsbook.pdf (accessed May 29, 2025).

[5] J. Cui, T. R. Liu, and R. Smith, D. "Introduction to metamaterials," in *Metamaterials*, J. Cui, T. R. Smith, D. and R. Liu, Eds. Boston, MA: Springer, 2010. [Online]. Available: https://doi.org/10.1007/978-1-4419-0573-4_1

[6] D. Sievenpiper, "High-impedance electromagnetic surfaces with a forbidden frequency band," *IEEE Transactions on Microwave Theory and Techniques*, vol. 47, no. 11, pp. 2059–2074, Nov. 1999.

[7] X. Ma, M. Pu, X. Li, Y. Guo, P. Gao, and X. Luo, "Meta-chirality: Fundamentals, construction and applications," *Nanomaterials*, vol. 7, no. 5, p. 116, May 2017.

[8] N. Inomata, T. Takahashi, Y. Sakai, T. Okatani, and Y. Kanamori, "Fabrication and application of 3d terahertz metamaterials with vertical multinanogaps for spectroscopic sensing," *Scientific Reports*, vol. 15, 2025.

[9] H. Chen, W. J. Padilla, J. M. O. Zide, A. C. Gossard, A. J. Taylor, and R. D. Averitt, "Active terahertz metamaterial devices," *Nature Photonics*, vol. 1, pp. 41–48, 2006.

[10] S. Dunst and P. Tomancak, "Imaging flies by fluorescence microscopy: Principles, technologies, and applications," *Genetics*, vol. 211, no. 1, pp. 15–34, January 2019, license: CC BY 4.0.

[11] B. Choudhury and R. M. Jha, "A review of metamaterial invisibility cloaks," *Computers, Materials & Continua*, vol. 33, no. 3, pp. 275–308, 2013. [Online]. Available: https://www.techscience.com/cmc/v33n3/22655

[12] T. Geetharamani, G.; Aathmanesan, "Design of metamaterial antenna for 2.4 ghz wifi applications," *Wireless Personal Communications 2020-apr 15 vol. 113 iss. 4*, vol. 113, apr 2020. [Online]. Available: libgen.li/file.php?md5=56aff72bd9fbd913a7c7b55f52a1cf27

[13] J. Song, L. Wang, M. Li, and J. Dong, "A dualband metamaterial absorber with adjacent absorption peaks," *Journal of Physics D: Applied Physics*, vol. 51, p. 385105, 2018.

[14] M. Hamza, Y. Abdulkarim, S. Saeed, M. Hamad, F. Muhammadsharif, M. Bakır, B. Appasani, and S. Haxha, "A very compact metamaterial-based triple-band sensor in terahertz spectrum as a perfect absorber for human blood cancer diagnostics," *Plasmonics*, 2024, advance online publication.

[15] Y. Zhou, Z. Qin, Z. Liang, D. Meng, H. Xu, D. R. Smith, and Y. Liu, "Ultra-broadband metamaterial absorbers from long to very long infrared regime," *Light: Science Applications*, vol. 10, p. 138, 2021.

[16] B. Qi, Y. Zhao, T. Niu, and Z. Mei, "Ultra-broadband metamaterial absorber based on all-metal nanostructures," *Journal of Physics D: Applied Physics*, vol. 52, no. 42, August 2019.

[17] Rajni and A. Marwaha, "An accurate approach of mathematical modeling of srr and sr for metamaterials," *[Journal/Conference]*, 2016, received 1 August 2016; Accepted 13 December 2016.

[18] D. C. Vikrant Thakur, "Metamaterials: A leading edge of science and technology," *International Journal of Computer Applications*, vol. 98, no. 9, pp. 29–34, July 2014. [Online]. Available: https://ijcaonline.org/archives/volume98/number9/17213-7441/

[19] A. Ali, A. Mitra, and B. Aïssa, "Metamaterials and metasurfaces: A review from the perspectives of materials, mechanisms and advanced metadevices," *Nanomaterials*, vol. 12, no. 6, 2022. [Online]. Available: https://www.mdpi.com/2079-4991/12/6/1027

[20] A. F. Mota and B.-H. V. Borges, "Improved homogenization procedure based on a drude–lorentz dispersive model for metamaterials," *Microwave and Optical Technology Letters*, vol. 58, no. 6, pp. 1490–1494, 2016. [Online]. Available: https://onlinelibrary.wiley.com/doi/abs/10.1002/mop.29813

[21] T. Amemiya, A. Ishikawa, T. Kanazawa, J. Kang, N. Nishiyama, Y. Miyamoto, T. Tanaka, and S. Arai, "Permeability-controlled optical modulator with tri-gate metamaterial: control of permeability on inp-based photonic integration platform," *Scientific Reports*, vol. 5, no. 1, p. 8985, 2015. [Online]. Available: https://doi.org/10.1038/srep08985

[22] J. Sun and J. Zhou, "Metamaterials: The art in materials science," *Engineering*, vol. 44, pp. 145–161, 2025. [Online]. Available: https://www.sciencedirect.com/science/article/pii/S2095809924007288

[23] C. Watts, X. Liu, and W. Padilla, "Metamaterial electromagnetic wave absorbers," *Advanced materials (Deerfield Beach, Fla.)*, vol. 24, pp. OP98–120, OP181, 06 2012.

[24] H.-L. Huang, H. Xia, Z.-B. Guo, D. Xie, and H.-J. Li, "Design of broadband metamaterial absorbers for permittivity sensitivity and solar cell application," *Chinese Physics Letters*, vol. 34, no. 11, p. 117801, 2017.

[25] Y. Bai, L. Zhao, D. Ju, Y. Jiang, and L. Liu, "Wide-angle, polarization-independent and dual-band infrared perfect absorber based on l-shaped

metamaterial," *Opt. Express*, vol. 23, no. 7, pp. 8670–8680, Apr 2015. [Online]. Available: https://opg.optica.org/oe/abstract.cfm?URI=oe-23-7-8670

[26] H. Cai, Y. Sun, X. Wang, S. Zhan *et al.*, "Design of an ultra-broadband near-perfect bilayer grating metamaterial absorber based on genetic algorithm," *Unpublished manuscript*, 2025, haoyuan Cai, Yi Sun, Xiaoping Wang, Shuyue Zhan, et al. (`shuyue_zhan@zju.edu.cn`).

[27] M. Faisal, A. U. Rahman, S. Khan, M. Siyaf, T. A. Shah, M. K. Okla, M. Bourhia, and Y. A. Younous, "Selective-wavelength perfect infrared absorption in ag@zno conical metamaterial structure," *Scientific Reports*, vol. 14, no. 1, p. 21321, 2024.

[28] X. Jia, S. Yin, and Z. Tang, "A simple metamaterial for high-performance spectrum-selective absorption in the visible region," *Symmetry*, vol. 14, no. 11, p. 2402, 2022.

[29] D. Wu, L. Lei, M. Xie, and P. Xu, "High-performance metamaterial light absorption from visible to near-infrared assisted by anti-reflection coating," *Photonics*, vol. 10, no. 9, p. 998, August 2023.

[30] F. Xu, L. Lin, J. Fang, M. Huang, F. Wang, J. Su, S. Li, and M. Pan, "Broadband solar absorber based on square ring cross arrays of zns," *Micromachines*, vol. 12, no. 8, p. 909, July 2021.

[31] nanoComposix. Gold nanoparticles: Optical properties. [Online]. Available: https://nanocomposix.com/pages/gold-nanoparticles-optical-properties

[32] L. Sito, A. Danisi, B. Salvant, and C. Zannini, "Mitigating the beam coupling impedance in accelerator components," CERN, Presentation, 8 2023, presentation at CERN. [Online]. Available: https://indico.cern.ch/event/1314348/contributions/5528629/attachments/2706143/4699142/MTM@CEI_31082023.pdf

[33] RefractiveIndex.Info. Optical constants of sic (silicon carbide). Contains data from Wang et al. (2013) *Laser Photonics Rev.* 7, 831-838. [Online]. Available: https://refractiveindex.info/?shelf=main&book=SiC&page=Wang-4H-e

[34] A. M. Ali, A. M. Ghanim, M. Othman, and M. A. Swillam, "All silicon mir super absorber using fractal metasurfaces," *Scientific Reports*, vol. 13, no. 1, p. 15545, 2023. [Online]. Available: https://doi.org/10.1038/s41598-023-42723-9

[35] P. Gómez García and J.-P. Fernández-Álvarez, "Floquet-bloch theory and its application to the dispersion curves of nonperiodic layered systems," *Mathematical Problems in Engineering*, vol. 2015, no. 1, p. 475364, 2015. [Online]. Available: https://onlinelibrary.wiley.com/doi/abs/10.1155/2015/475364

[36] J.-P. Berenger, "A perfectly matched layer for the absorption of electromagnetic waves," *Journal of Computational Physics*, vol. 114, no. 2, pp. 185–200, 1994. [Online]. Available: https://www.sciencedirect.com/science/article/pii/S0021999184711594

[37] O. Schenk and K. Gärtner, *PARDISO User Guide Version 7.2*, PARDISO Project, December 2020, updated December 28, 2020. [Online]. Available: https://community.intel.com/cipcp26785/attachments/cipcp26785/oneapi-math-kernel-library/31031/1/manual.pdf
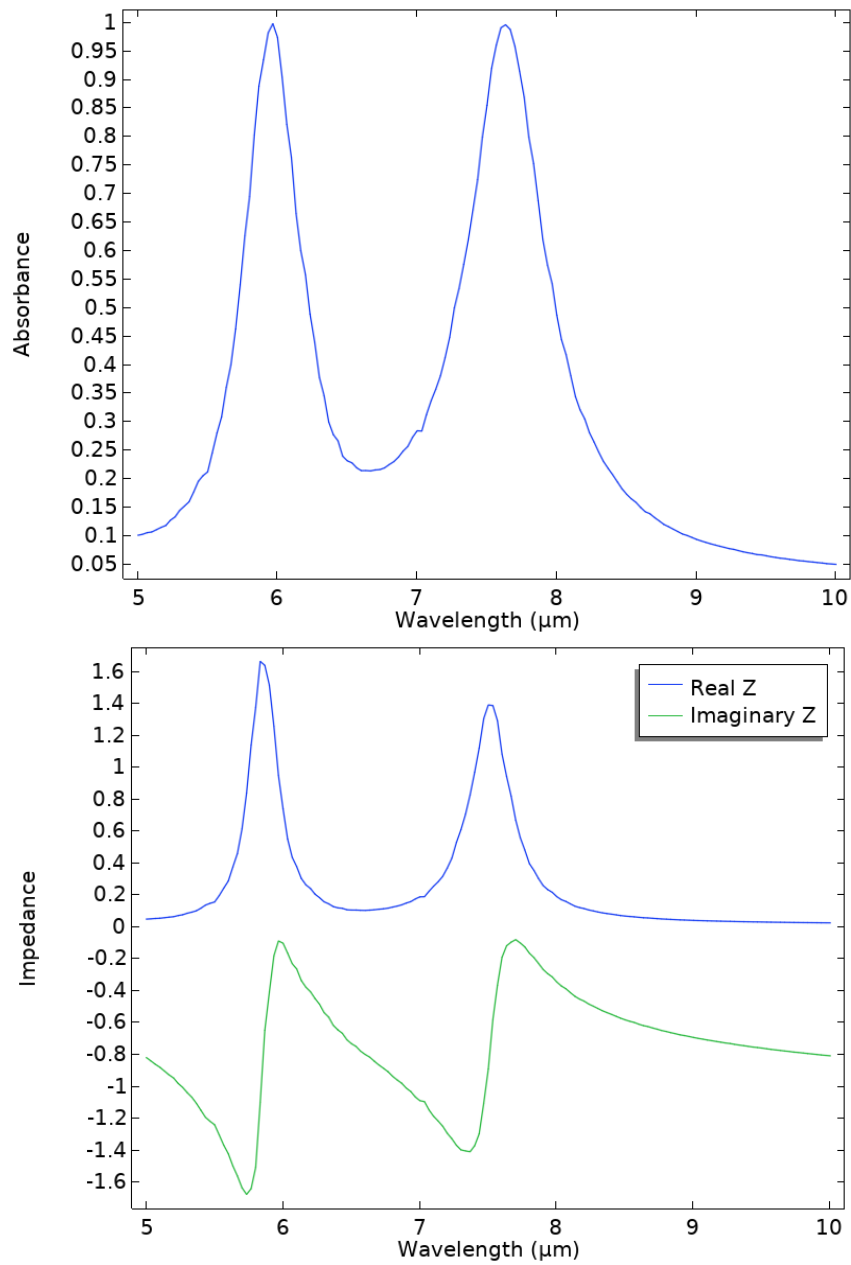
Appendix A

A.1 Replication of Yang Bai *et al.* Work

Figure A.1: Replication of Yang Bai *et al.* work in Comsol Multiphysics.

A.2 Initial Designs of Metamaterial Absorber
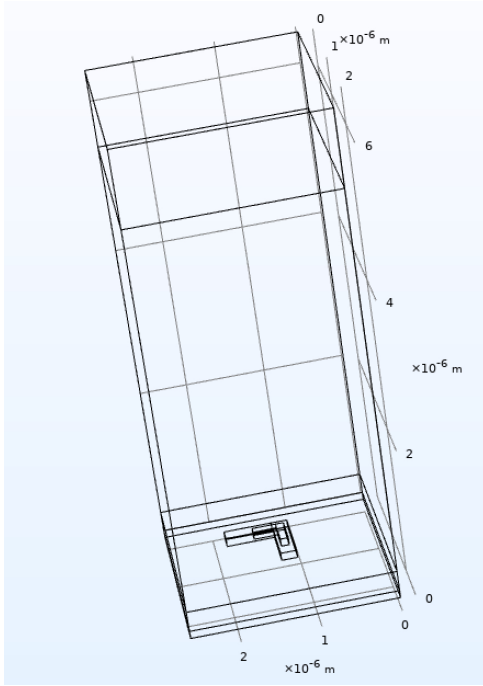
1. **Nested L shape :**

Figure A.2: Side view of the nested L structure.
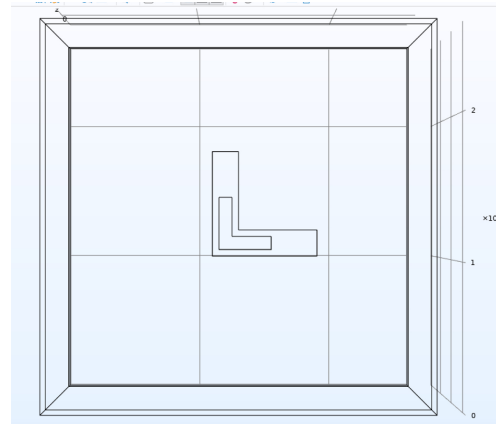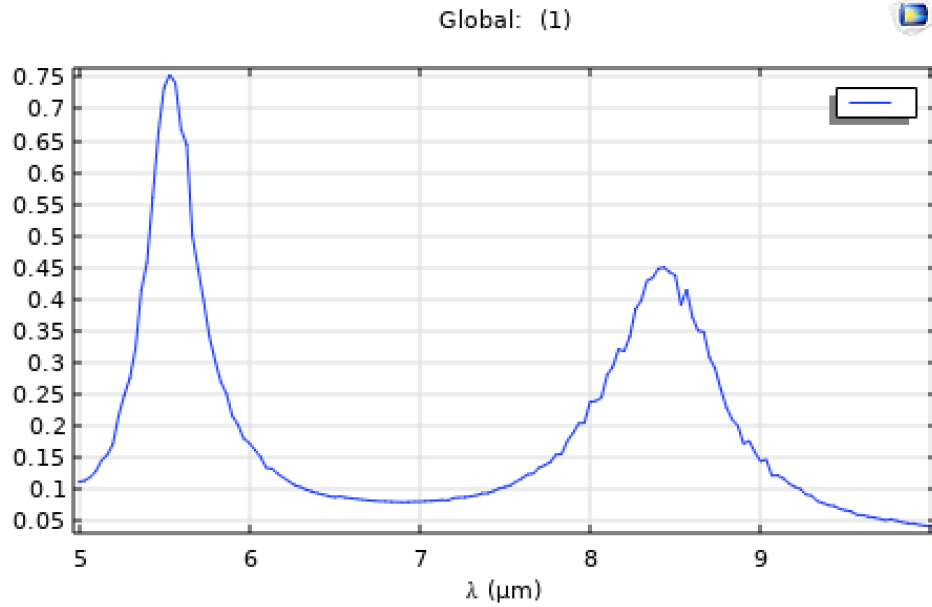

Figure A.3: Top view of the nested L structure.

Figure A.4: Absorption curve of the nested L structure, showing two peaks. The max absorbtion is 75%
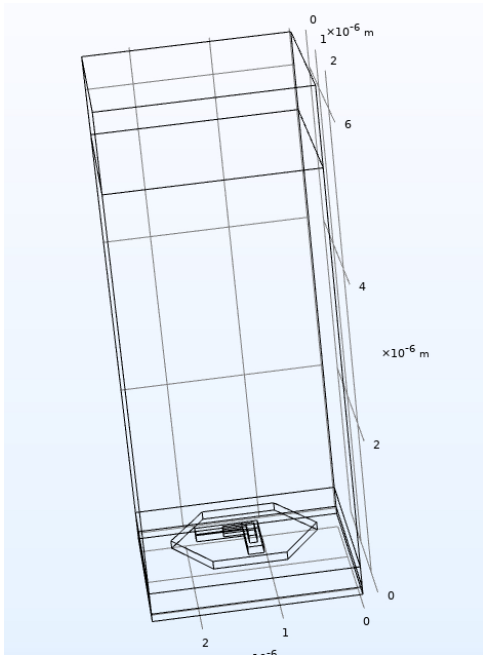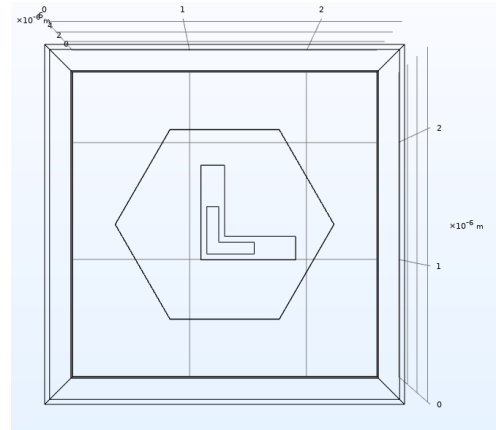
2. **Hexagon-Nested L shape:**

Figure A.5: Side view of the Hexagon nested L structure.

Figure A.6: Top view of the Hexagon nested L structure.
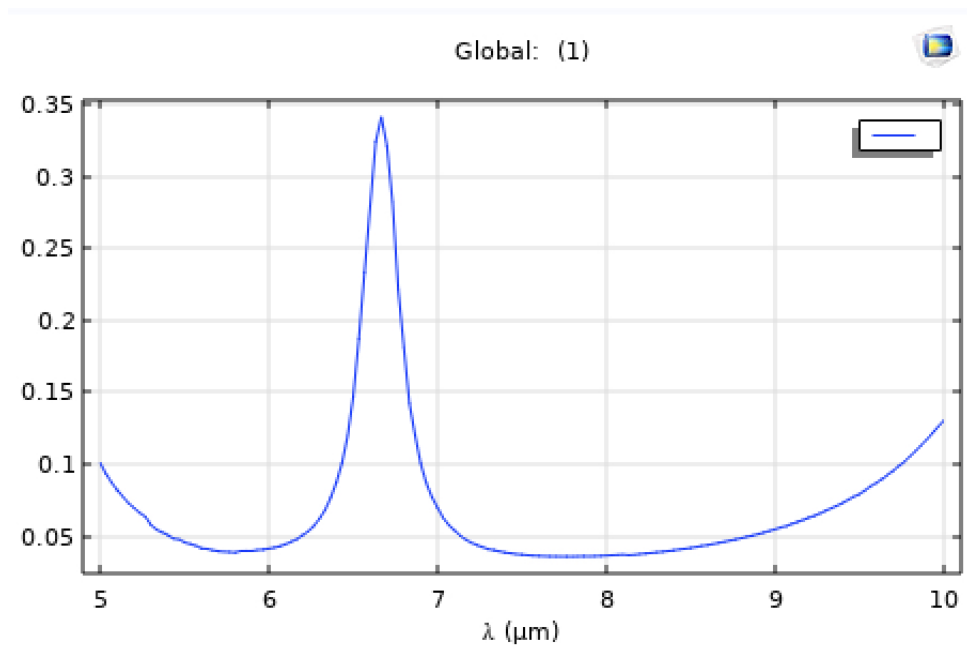
Figure A.7: Absorption curve of the Hexagon Nested L structure, showing only 1 peak. with almost no absorbtion.
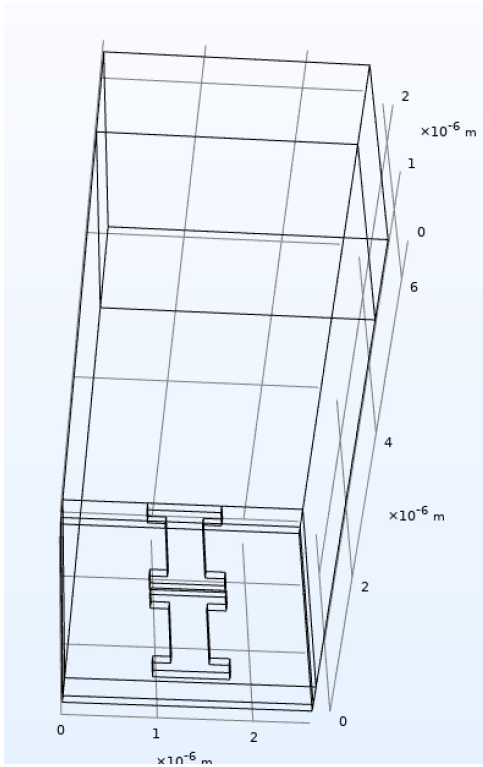
3. **Double I structre**

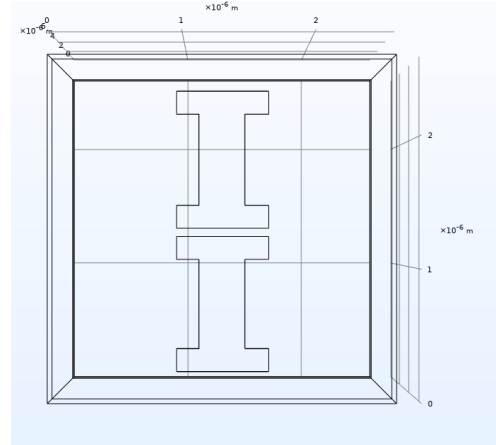Figure A.8: Side view of the double I structure.
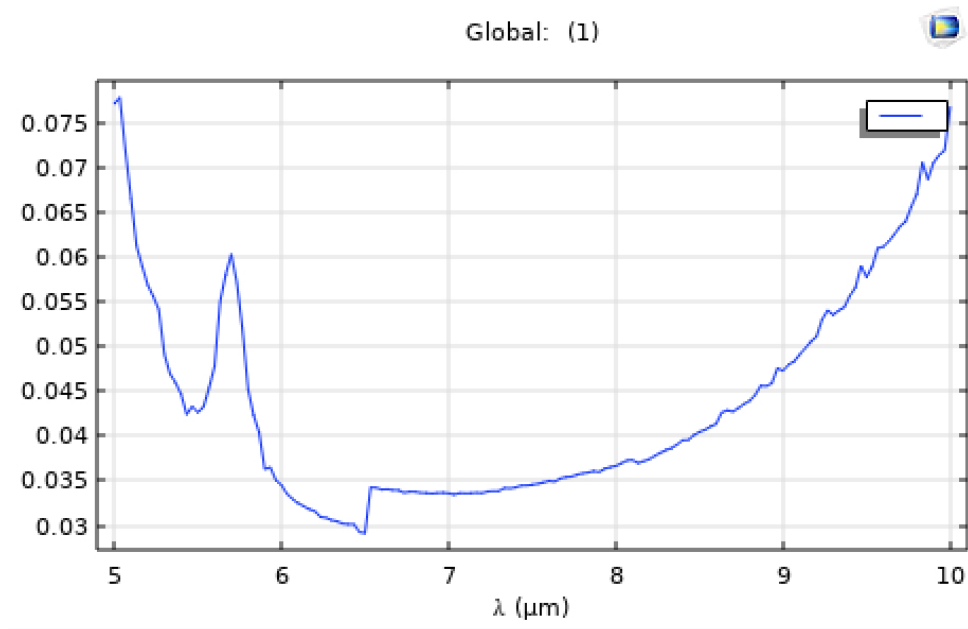

Figure A.9: Top view of the double I structure.

Figure A.10: Absorption curve of the double I structure, showing 1 only peak. with almost no absorbtion.
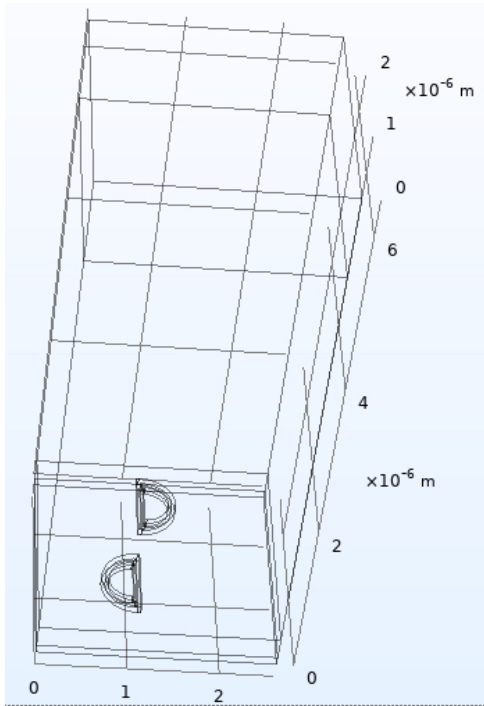
4. Double D structure :

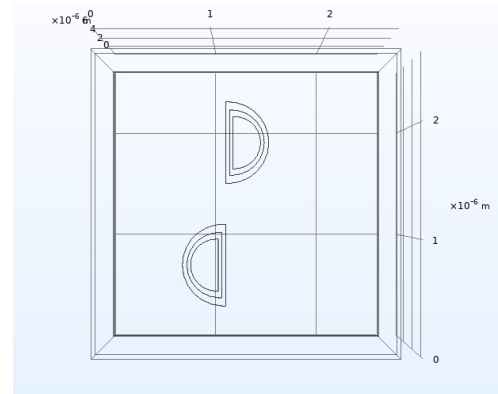Figure A.11: Side view of the double D structure.
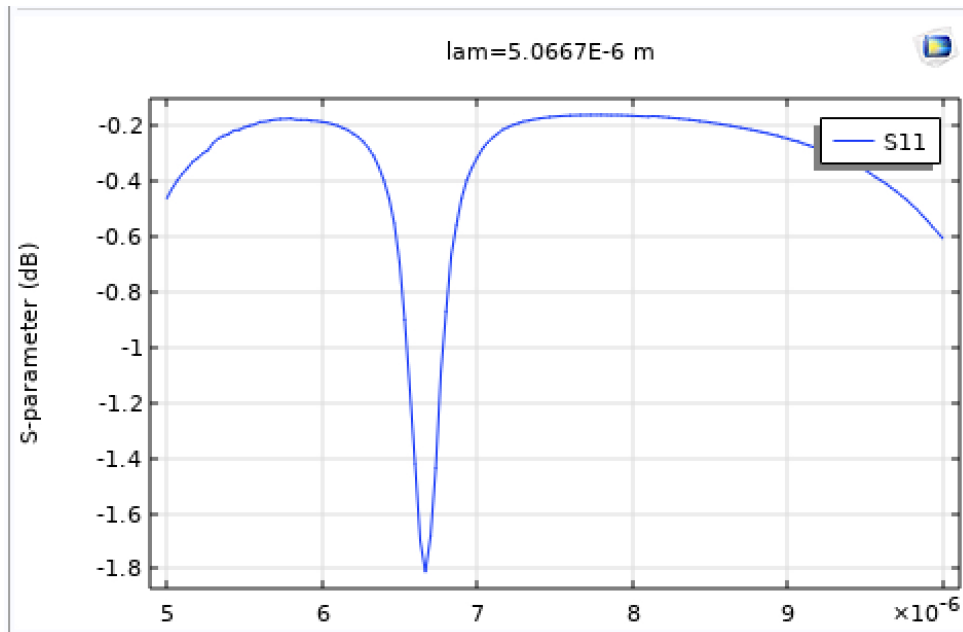

Figure A.12: Top view of the double D structure.

Figure A.13: Reflection curve (S11 parameter in dB scale) of the double D structure, showing only 1 peak. with almost no absorbtion.

A.3   Plagiarism Report

main.pdf

Delhi Technological University

Document Details

Submission ID

trn:oid:::27535:99689742

Submission Date

Jun 6, 2025, 9:20 PM GMT+5:30

Download Date

Jun 6, 2025, 9:24 PM GMT+5:30

File Name

main.pdf

File Size

18.9 MB

60 Pages

11,893 Words

65,051 Characters

8% Overall Similarity

The combined total of all matches, including overlapping sources, for each database.

Filtered from the Report

▸ Bibliography

▸ Small Matches (less than 10 words)

Exclusions

▸ 3 Excluded Matches

Match Groups

46 Not Cited or Quoted 7%
Matches with neither in-text citation nor quotation marks

5 Missing Quotations 1%
Matches that are still very similar to source material

3 Missing Citation 1%
Matches that have quotation marks, but no in-text citation

0 Cited and Quoted 0%
Matches with in-text citation present, but no quotation marks

Top Sources

6% 🌐 Internet sources

4% 📖 Publications

5% 👤 Submitted works (Student Papers)

Integrity Flags

2 Integrity Flags for Review

🚩 **Replaced Characters**
86 suspect characters on 28 pages
Letters are swapped with similar characters from another alphabet.

🚩 **Hidden Text**
2 suspect characters on 2 pages
Text is altered to blend into the white background of the document.

Our system's algorithms look deeply at a document for any inconsistencies that would set it apart from a normal submission. If we notice something strange, we flag it for you to review.

A Flag is not necessarily an indicator of a problem. However, we'd recommend you focus your attention there for further review.

Match Groups

46 Not Cited or Quoted 7%
Matches with neither in-text citation nor quotation marks

5 Missing Quotations 1%
Matches that are still very similar to source material

3 Missing Citation 1%
Matches that have quotation marks, but no in-text citation

0 Cited and Quoted 0%
Matches with in-text citation present, but no quotation marks

Top Sources

6% 🌐 Internet sources

4% 📖 Publications

5% 👤 Submitted works (Student Papers)

Top Sources

The sources with the highest number of matches within the submission. Overlapping sources will not be displayed.

1	Internet	
de.overleaf.com		**<1%**

2	Internet	
dspace.dtu.ac.in:8080		**<1%**

3	Internet	
en.wikipedia.org		**<1%**

4	Publication	
Ben-Xin Wang, Chongyang Xu, Guiyuan Duan, Wei Xu, Fuwei Pi. "Review of Broad...		**<1%**

5	Submitted works	
The University of Memphis on 2013-10-03		**<1%**

6	Publication	
Gao, Yun. "Graphene Optoelectronic Devices on Silicon Nitride Waveguide Platfor...		**<1%**

7	Internet	
arcadia.sba.uniroma3.it		**<1%**

8	Internet	
www.mdpi.com		**<1%**

9	Internet	
onlinelibrary.wiley.com		**<1%**

10	Submitted works	
Stony Brook University on 2024-09-08		**<1%**

11 Submitted works

Delhi Technological University on 2019-10-30   **<1%**

12 Internet

www.osapublishing.org   **<1%**

13 Internet

www.vaia.com   **<1%**

14 Internet

ipindexing.com   **<1%**

15 Internet

academic.hep.com.cn   **<1%**

16 Internet

emlab.utep.edu   **<1%**

17 Publication

Ceraolo, . "The Fundamental Laws of Electromagnetism", Fundamentals of Electri...   **<1%**

18 Internet

engineering.purdue.edu   **<1%**

19 Publication

Fuyin Luo, Chuanliang Li, Xiaohu He. "Ultra-wideband and wide-angle metamater...   **<1%**

20 Internet

acp.copernicus.org   **<1%**

21 Internet

ebin.pub   **<1%**

22 Internet

pdffox.com   **<1%**

23 Publication

Mohamed Edries, Hesham A. Mohamed, Sherif S. Hekal, Mohamed A. El-Morsy, Ha...   **<1%**

24 Internet

index-of.es   **<1%**

25 **Publication**

Haoyuan Cai, Yi Sun, Xiaoping Wang, Shuyue Zhan. "Design of an ultra-broadban... <1%

26 **Publication**

Hodjat Hajian, Amir Ghobadi, Bayram Butun, Ekmel Ozbay. "Active metamaterial ... <1%

27 **Publication**

Mahesh Abegaonkar, Lalithendra Kurra, Shiban Kishen Koul. "Printed Resonant P... <1%

28 **Submitted works**

Manipal University on 2016-10-24 <1%

29 **Submitted works**

Middle East Technical University on 2016-08-08 <1%

30 **Publication**

Nasrollah Karampour, Najmeh Nozhat. "Ultra-wideband polarization insensitive ... <1%

31 **Submitted works**

University of Glasgow on 2011-08-22 <1%

32 **Submitted works**

University of Liverpool on 2024-01-08 <1%

33 **Internet**

dspace.cuni.cz <1%

34 **Internet**

kth.diva-portal.org <1%

35 **Internet**

pubs.rsc.org <1%

36 **Internet**

www.ebooks.com <1%

A.4 Conference Certificate

ATMA RAM SANATAN DHARMA COLLEGE
UNIVERSITY OF DELHI

Accredited Grade 'A++' By NAAC || All India 5th Rank in NIRF (Ministry of Education)

3rd International Conference on

Advanced Functional Materials and Devices (AFMD-2025)
for Sustainable Development

Under the aegis of IQAC and supported by Department of Biotechnology (GoI)

Certificate of Participation

This is to certify that Prof./Dr./Mr./Ms.

BHAVAY LUTHRA

DELHI TECHNOLOGICAL UNIVERSITY

has participated in the 3rd International Conference on "Advanced Functional Materials & Devices for Sustainable Development" (AFMD-2025) organised by Department of Physics under the aegis of IQAC ARSD College, University of Delhi, India during March 03-05, 2025 in hybrid mode.

He/She has presented **Poster** entitled:

PP-69:-Broadband Multi-Patterned Metamaterial Absorber for Mid-Infrared Region

Dr. Shankar Subramanian	**Dr. Anjali Sharma**	**Prof. Vinita Tuli**	**Prof. Gyantosh Kumar Jha**
Convener, AFMD-2025	Convener, AFMD-2025	Coordinator, IQAC	Principal/Patron AFMD-2025

Certificate No: ARSD/AFMD25/PP/072

A.5 Indexing Proof

JOURNAL OF ELECTRONIC MATERIALS

Publisher: SPRINGER , ONE NEW YORK PLAZA, SUITE 4600 , NEW YORK, United States, NY, 10004

ISSN / eISSN: 0361-5235 / 1543-186X

Web of Science Core Collection: **Science Citation Index Expanded**

Additional *Web of Science* Indexes: **Current Contents Electronics & Telecommunications Collection | Current Contents Physical, Chemical & Earth Sciences | Essential Science Indicators**

< Share This Journal   **View profile page**

A.6   Journal Submission Status

Journal of Electronic Materials
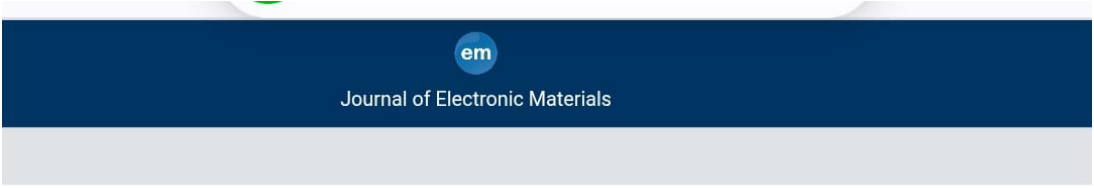
missions Being Processed for Author

1 (1 total submissions)   Results per page 10 ⌄

		Manuscript Number ▲	Title ▲	Initial Date Submitted ▼	Status Date ▲	Current Status ▲
ubmission pondence -mail		JEMS-D-25-01221	Broadband Multi-Patterned Metamaterial Absorber for Mid-Infrared Region	22 May 2025	04 Jun 2025	Reviews Completed

1 (1 total submissions)   Results per page 10 ⌄